Original Article | **Open Access**

Extracellular Vesicles and Circulating Nucleic Acids

Zhang *et al. Extracell Vesicles Circ Nucleic Acids.* 2026;7:1863-94 **DOI:**10.20517/evcna.2026.149

Mesenchymal stem cell-derived extracellular vesicles promote macrophage efferocytosis and inflammation resolution in osteoarthritis through the miR-21a-5p/YAP1 axis

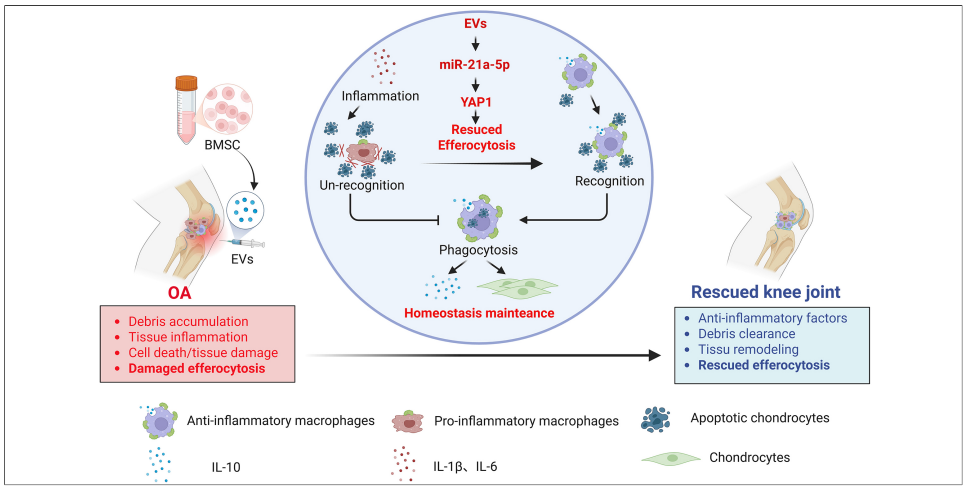
Lei Zhang[1,#], Yaguang Han[1,#], Shu Chen[1,#], Kaiqiang Sun[1,2], Zhenyu Gong[3,4], Jia Cao[1], Jinhui Peng[1], Bo Wang[1], Qi Zhou[1], Peiliang Fu[1], Qirong Qian[1], Yiqin Zhou[1]

Keywords:
Osteoarthritis, extracellular vesicles, macrophage efferocytosis, miR-21a-5p, YAP1, mesenchymal stem cells

Citation: Zhang L, Han Y, Chen S, Sun K, Gong Z, Cao J, Peng J, Wang B, Zhou Q, Fu P, Qian Q, Zhou Y. Mesenchymal stem cell-derived extracellular vesicles promote macrophage efferocytosis and inflammation resolution in osteoarthritis through the miR-21a-5p/YAP1 axis. *Extracell Vesicles Circ Nucleic Acids.* 2026;7:1863-94. https://dx.doi.org/10.20517/evcna.2026.149

Received: 10 Jul 2026
First Decision: 19 Aug 2026
Revised: 9 Sep 2026
Accepted: 21 Sep 2026
Published: 22 Oct 2026

Academic Editors: Yoke Peng Loh, Zhaohui Huang
Copy Editor: Ting-Ting Hu
Production Editor: Ting-Ting Hu



Abstract

Aim: Osteoarthritis (OA) involves chronic inflammation and cartilage degeneration. Impaired macrophage efferocytosis may contribute to OA progression. This study investigated whether mesenchymal stem cell-derived extracellular vesicles (MSC-EVs) enhance macrophage efferocytosis and inflammation resolution in OA.

Methods: Human OA-associated macrophage populations were analyzed using single-cell RNA-sequencing data (GSE220243). *In vitro* co-culture models combining bone marrow-derived macrophages with apoptotic chondrocytes were used to assess efferocytosis and inflammatory responses. microRNA (miRNA) profiling, luciferase assays, and functional experiments were performed to investigate the miR-21a-5p/YAP1 pathway. Therapeutic effects were assessed using a murine model of medial meniscus destabilization (DMM).

Results: Reanalysis of a single-cell transcriptomic dataset revealed an increased proportion of pro-inflammatory macrophage populations and reduced efferocytosis-related signatures

[1]Department of Orthopedics, Shanghai Changzheng Hospital, Naval Medical University, Shanghai 200003, China.
[2]Department of Orthopedics, Naval Medical Center of PLA, Shanghai 200052, China.
[3]Department of Neurosurgery/Neuro-Oncology, State Key Laboratory of Oncology in South China, Guangdong Provincial Clinical Research Center for Cancer, Sun Yat-Sen University Cancer Center, Guangzhou 510060, Guangdong, China.
[4]Department of Neurosurgery, Klinikum Rechts der Isar, Technische Universität München, Munich 81675, Germany.
[#]These authors contributed equally to this work.

Correspondence to: Prof. Qirong Qian, Prof. Yiqin Zhou, Department of Orthopedics, Shanghai Changzheng Hospital, Naval Medical University, Shanghai 200003, China. E-mail: qianqr@smmu.edu.cn; drzhouyiqin@163.com

in OA samples. Mesenchymal stem cell-derived extracellular vesicles (MSC-EVs) enhanced macrophage efferocytosis, promoted a pro-resolving inflammatory phenotype, and attenuated chondrocyte damage *in vitro*. miR-21a-5p was identified as a highly abundant miRNA in MSC-EVs and was reduced in OA human samples. MSC-EV exposure increased miR-21a-5p abundance in macrophages, while miR-21a-5p directly targeted the Yap1 3′-untranslated region (3′-UTR) and modulated efferocytosis-related gene expression, including Gas6, Mertk, and Stab2. YAP1 overexpression counteracted these effects. In the DMM model, MSC-EV treatment and intra-articular administration of miR-21a-5p mimic reduced osteophyte formation, preserved cartilage architecture, lowered Osteoarthritis Research Society International (OARSI) and synovitis scores, and improved inflammatory and efferocytosis-related molecular profiles. Together, these findings support a functional contribution of the miR-21a-5p/YAP1 axis to MSC-EV-associated macrophage regulation and OA protection.

Conclusion: MSC-EVs promote macrophage efferocytosis and joint protection in OA through the miR-21a-5p/YAP1 pathway, providing a potential therapeutic strategy for inflammation resolution.

INTRODUCTION

Osteoarthritis (OA) is a major global contributor to chronic joint pain and functional disability, marked by progressive cartilage degeneration, synovial inflammation, and subchondral bone remodeling[1,2]. Although the disease imposes a significant burden, existing treatments primarily aim at managing symptoms instead of altering the disease's fundamental progression[1]. Increasing evidence highlights immune dysregulation, particularly macrophage-driven inflammation, as an important contributor to OA pathogenesis[3,4]. Macrophages within the synovial microenvironment display significant phenotypic plasticity, adopting either pro-inflammatory or anti-inflammatory states that are crucial for tissue homeostasis and repair[5]. Efferocytosis, the macrophage-driven removal of apoptotic cells, plays a crucial role in resolving inflammation. Impairment of this process may promote the persistence of apoptotic chondrocytes, secondary necrosis, and sustained inflammatory signaling, thereby contributing to OA progression[6,7]. Although the role of macrophage efferocytosis in resolving inflammation is increasingly recognized, its contribution to OA pathogenesis and joint homeostasis remains incompletely understood.

Bone marrow mesenchymal stem cells (BMSCs) have attracted significant interest in regenerative medicine due to their immunomodulatory and trophic characteristics[8]. Growing evidence indicates that therapeutic effects are primarily mediated by paracrine signaling, with extracellular vesicles (EVs) playing a crucial role in this mechanism[9-11]. MSC-EVs are nanoscale vesicles containing bioactive molecules, such as proteins, lipids, and nucleic acids, facilitating intercellular communication[9-11]. MSC-EVs have been demonstrated to influence macrophage polarization, encouraging a transition to an anti-inflammatory phenotype[12,13]. However, the role of BMSC-derived EVs in regulating macrophage efferocytosis in OA, as well as the underlying molecular mechanisms, remains incompletely understood.

MicroRNAs (miRNAs) are important regulators of OA pathogenesis, influencing chondrocyte metabolism, synovial fibrosis, and inflammatory responses[14]. Numerous miRNAs are involved in macrophage polarization, influencing the equilibrium between pro-inflammatory and anti-inflammatory phenotypes[15-17]. However, the involvement of specific miRNAs in macrophage efferocytosis in OA remains poorly defined. Likewise, although MSCs are known to modulate immune responses, whether BMSCs enhance macrophage efferocytosis through EV-associated miRNA signaling has not been fully established. MSC-EVs can carry bioactive molecules, including miRNAs, and contribute to intercellular communication[18,19], with therapeutic

effects reported in a range of inflammatory conditions[18,19]. Nevertheless, it remains unclear whether BMSCs regulate macrophage efferocytosis through EV-associated signaling, which miRNAs are involved, and how these pathways operate within the OA microenvironment.

We combined single-cell transcriptomic analysis with functional *in vitro* assays and *in vivo* validation to address these questions. Our findings revealed that impaired macrophage efferocytosis is associated with enhanced inflammatory responses and tissue damage in OA. We identified miR-21a-5p as a prevalent miRNA in MSC-EVs and examined its role in regulating macrophage efferocytosis. YAP1 was identified as a downstream target of miR-21a-5p.Our findings suggest that EV-associated miR-21a-5p/YAP1 signaling plays a role in modulating macrophage function, although the direct transfer of miR-21a-5p via EVs requires further confirmation.

METHODS

Data acquisition and processing

Human knee single-cell RNA sequencing (scRNA-seq) data, accessible under accession number GSE220243, were sourced from the Gene Expression Omnibus (GEO) database[20]. The dataset includes tissues from healthy and OA knees, specifically healthy articular cartilage (n = 6), OA articular cartilage (n = 6), healthy meniscus (n = 7 donors), and OA meniscus (n = 6 donors). A total of 26 scRNA-seq libraries are included in the GEO series, with the vascular and avascular regions of the meniscus from one healthy donor analyzed separately. No synovial tissue samples are included in GSE220243.

The analytical workflow was performed according to established procedures as previously described. Quality control measures excluded low-quality cells with feature counts outside 200-6,000 or mitochondrial/ribosomal transcript proportions over 10%.To minimize technical variability from sequencing depth and cellular heterogeneity, the retained cells underwent normalization and scaling using the NormalizeData and ScaleData functions. Principal component analysis (PCA) was performed on the identified highly variable features to reduce dimensionality. To minimize inter-sample batch effects, data integration was performed using the RunHarmony function implemented in the Harmony package. The integrated dataset was visualized using Uniform Manifold Approximation and Projection (UMAP), and major cell populations were annotated based on the expression of established lineage-specific marker genes, referencing the CellMarker database (http://bio-bigdata.hrbmu.edu.cn/CellMarker/).

Pseudotime analysis

Monocle2 (version 2; http://cole-trapnell-lab.github.io/monocle-release/) was employed for single-cell trajectory reconstruction. Dimensionality reduction was performed to capture major transcriptional variation among cells, followed by cell ordering along the inferred pseudotime trajectory. This analysis enabled the characterization of transcriptional state transitions and branch points associated with differentiation or activation processes.

Kyoto Encyclopedia of Genes and Genomes pathway enrichment analysis

Differential expression analysis utilized the 'limma' R package, applying a significance threshold of $P < 0.05$[21]. The biological functions of identified differentially expressed genes (DEGs) in cell clusters were analyzed using the 'org.Hs.eg.db' and 'clusterProfiler' packages. A Kyoto Encyclopedia of Genes and Genomes (KEGG) pathway enrichment analysis was conducted to identify significantly enriched pathways, applying a P value threshold of 0.05.

Score according to polarization-related hallmark genes

Single-cell macrophage efferocytosis-related gene-set activity was quantified using AUCell, which employs area-under-the-curve (AUC) enrichment scores. Gene sets were sourced from the Hallmark collection in the Molecular Signatures Database (MSigDB; https://www.gsea-msigdb.org/). M1- and M2-associated transcriptional programs were similarly evaluated across macrophage subtypes using the corresponding gene signatures, and their relative activities were compared on the basis of AUC scores.

Human knee-joint tissue acquisition

Samples of cartilage, synovial tissue, and synovial fluid were collected from 10 healthy controls and 10 osteoarthritis patients [Supplementary Table 1]. Normal-control specimens were collected during arthroscopic procedures for acute anterior cruciate ligament rupture or meniscal injury, while OA specimens were obtained from total knee arthroplasty patients. Subjects were excluded before experimental allocation if they had a history of bone fracture, previous knee surgery, including arthroplasty, ligament reconstruction, or cartilage repair, or inadequate clinical imaging quality. Following confirmation of eligibility, specimens were coded and allocated to the planned downstream assays. When only five specimens were required for a particular assay, five cases were randomly selected from the eligible cohort before experimental analysis. The study involving human specimens was reviewed and approved by the Human Ethics Committee of Changzheng Hospital (Approval No. SL202410-7A). Written informed consent was obtained from all participants before sample collection.

Isolation and culture of primary mouse BMSCs, bone marrow-derived macrophages (BMDMs) and chondrocytes

Primary BMSCs were obtained and cultured as previously described[22]. C57BL/6 mice, aged one month, were euthanized through cervical dislocation and surface-sterilized by immersing them in 75% ethanol for 5 min. The sex of the donor mice was not specified. Femurs and tibias were aseptically dissected and transferred to ice-cold phosphate-buffered saline (PBS, G4202, Servicebio) supplemented with 1% penicillin-streptomycin (P/S; G4003, Servicebio). The bone epiphyses were excised to reveal the medullary cavities, which were then flushed with Dulbecco's Modified Eagle Medium (DMEM)/F-12 medium (Gibco, 12634028) supplemented with 20% fetal bovine serum (FBS) (ZETAlife, Z7010FBS) and 1% P/S, using a 1 mL syringe equipped with a 25-gauge needle. The bone marrow was collected, homogenized by pipetting, and filtered through a 75 μm cell strainer to create a single-cell suspension. Cells were resuspended and seeded into T25 culture flasks, then incubated at 37 °C with 5% CO_2. After 24 h, non-adherent cells were removed by aspiration, and fresh complete medium was replenished. The medium was first replaced at 72 h and then every 48 h thereafter. Cells at around 80% confluency were detached with 0.25% Trypsin-ethylenediaminetetraacetic acid (EDTA) (G3440, Servicebio) for subculturing. Phenotypic surface biomarkers were identified using flow cytometry (CytoFlex, A00-1-1102, XItogen Biotechnologies Co., Ltd., China). According to the manufacturer's protocols, BMSCs exhibited positive biomarkers CD44 (949601, BioLegend), CD29 (102201, BioLegend), and CD90 (105201, BioLegend), while negative biomarkers included CD11b (101203, BioLegend) and CD45 (157202, BioLegend). Third-passage cells were utilized for subsequent experiments.

BMDMs were extracted from the long bones of one-month-old C57BL/6 mice post-euthanasia. The marrow cavity was flushed under sterile conditions with a syringe after excising the epiphyses of the tibiae and femurs. The collected cells were resuspended and seeded into culture flasks. Bone marrow cells were cultured in 10-cm dishes using DMEM (Gibco, 11965092) with 10% FBS, 1% penicillin-streptomycin, and 25 ng/mL macrophage colony-stimulating factor (M-CSF; GB310046, Servicebio). Cultures were maintained for 6 days, with medium replacement every 48 h.

Primary chondrocytes were extracted from neonatal C57BL/6 mouse knee articular cartilage using enzymatic digestion, following established methods[23]. The sex of the neonatal donor mice was not specified. Cartilage

tissues were minced into ~1 mm^3 fragments and digested sequentially with 0.25% trypsin for 30 min, then 0.2% type II collagenase for 4 h in a shaking incubator at 90 rpm. The isolated cells were cultured in DMEM/F12 medium (Gibco, 12634028) with 10% FBS (ZETAlife, Z7010FBS) and 1% P/S (Servicebio, G4003) at 37 °C in a 5% CO_2 humidified atmosphere. To preserve the chondrogenic phenotype, only cells within two passages were used for experiments.

Mycoplasma testing

Cultured cells were regularly screened for mycoplasma contamination using a PCR-based detection assay (C0301S, Beyotime Biotechnology, China) following the manufacturer's guidelines. Cells were tested before their use in downstream experiments and periodically during culture. Only mycoplasma-negative cultures were used for experimental analyses, as all cultures tested negative for mycoplasma.

Isolation and Identification of MSC-EVs

BMSCs were maintained in 10 cm dishes with exosome-depleted FBS (System Biosciences, USA, 50A-1) at 37 °C in a normoxic environment (21% O_2).MSC-EVs were extracted from conditioned medium using differential ultracentrifugation, following established protocols. Supernatants were centrifuged sequentially at 300 × *g* for 10 min, 2,000 × *g* for 10 min, and 10,000 × *g* for 30 min at 4 °C to eliminate cellular debris. The clarified medium underwent two rounds of ultracentrifugation at 100,000 × *g* for 70 min each at 4 °C. The resulting pellet was resuspended in PBS to obtain BMSC-derived MSC-EVs. Transmission electron microscopy (TEM) (HT7800/HT7700, Hitachi) was utilized for morphological characterization. Nanoparticle tracking analysis (NTA) with a Flow NanoAnalyzer N30E (China) was employed to assess the particle size distribution and concentration of MSC-EVs. The expression of exosome markers CD81, CD63, and TSG101 was assessed using Western blot analysis.

Efferocytosis assay

An efferocytosis assay was conducted following the method outlined in a previousstudy[6]. BMDM were cultured in 6-well plates at 1 × 10^6 cells per well and incubated overnight in DMEM with 10% FBS. Cells were subsequently treated for 24 or 48 h with lipopolysaccharide (LPS, 100 ng/mL), apoptotic chondrocytes, BMSCs, MSC-EVs (104 particles /cell), miR-21a-5p mimics, or Yes1-associated transcriptional regulator (*Yap1*)-OE. Chondrocytes underwent apoptosis induction via 24-h exposure to tumor necrosis factor alpha (TNF-α) (500 ng/mL), following the methodology outlined in a prior study[24]. Apoptotic chondrocytes labeled with carboxyfluorescein succinimidyl ester (CFSE) were co-cultured with macrophages at a 10:1 ratio for 120 min. After incubation, cells were washed three times with PBS to eliminate non-phagocytosed chondrocytes. Immunofluorescence (IF) microscopy was utilized to evaluate efferocytosis. The efferocytosis index was calculated by determining the percentage of macrophages with apoptotic bodies in relation to the total number of macrophages, then multiplying by 100%.

miRNA sequencing and abundance profiling

To characterize the miRNA cargo of BMSC-derived MSC-EVs and screen for highly abundant candidate miRNAs, one purified MSC-EV sample (n = 1) was subjected to high-throughput small RNA sequencing. RNA extraction from purified MSC-EVs was performed using TRIzol reagent following the manufacturer's guidelines. RNA quality and concentration were assessed before library preparation. Genekinder Medicaltech (Shanghai, China) provided technical support for small RNA library construction and high-throughput sequencing. Raw sequencing reads were subjected to quality control, including removal of adaptor sequences, low-quality reads, and other invalid reads. Clean reads were aligned to the mouse reference genome, and known miRNAs were identified by comparing them with annotated sequences in the miRBase database. miRNA levels were normalized to reads per million (RPM) by dividing individual miRNA reads by the total mapped miRNA reads and multiplying by 10^6. The miRNAs were then ranked by

normalized abundance, and the top ten were chosen for further validation via quantitative real-time polymerase chain reaction (RT-qPCR). Because only one MSC-EV sample was subjected to miRNA sequencing, this analysis was used exclusively for descriptive miRNA abundance profiling and candidate screening, rather than for differential-expression analysis or statistical inference.

miRNA transient transfection

In recipient-macrophage gain-of-function experiments, primary BMDMs were transfected with miR-21a-5p mimic or a non-targeting control (mimic-NC) using Lipofectamine™ 3000, following the manufacturer's protocol. Both the miR-21a-5p mimic and mimic-NC were sourced from Shanghai BioTNT Biotechnology Co., Ltd. 4 h post-transfection, the medium was refreshed with new growth medium, and the cells were subjected to the specified treatments involving LPS and/or Yap1 overexpression for further functional assays.

In the miR-21a-5p inhibition study, BMSCs were transfected with either a miR-21a-5p inhibitor or a non-targeting control (inhibitor-NC) using Lipofectamine™ 3000 for 24 h. Post-transfection, the cells were washed and maintained in an EV-depleted medium. The conditioned medium was collected, and EVs were isolated using differential ultracentrifugation as previously detailed. EV preparations derived from inhibitor-NC- or miR-21a-5p inhibitor-transfected BMSCs were subsequently applied to recipient BMDMs.

Plasmid transfection

The complete coding sequence of the Yes1-associated transcriptional regulator (Yap1; Gene ID 22601, NM_001171147.1) was synthesized and inserted into a Flag-tagged vector (PGMLV-6751) by BioTNT Biotechnology Co., Ltd. (Shanghai, China). Mouse primary BMDMs were transfected with the constructed plasmid using Lipofectamine™ 3000 reagent (Invitrogen) following the manufacturer's protocol. Cells were seeded at 6×10^4 per well in 6-well plates a day before transfection. The culture medium was replaced when the cells reached 80% confluency. A transfection mixture was prepared with 125 μL Opti-MEM® medium, 7.5 μL Lipofectamine3000™, 2,500 ng plasmid DNA, and 5 μL P3000™ reagent, then added to each well and incubated for 24 h. Finally, overexpression was assessed using RT-qPCR [Supplementary Figure 1].

Small interfering RNA (siRNA) for Yap1 transfection assay

Three siRNA sequences were designed in collaboration with BioTNT Biotechnology Co., Ltd. (Shanghai, China) to silence mouse Yap1 expression. Mouse primary BMDMs were transfected at 80% confluency in 12-well plates using Lipofectamine™ 3000 Reagent (Invitrogen) following the manufacturer's guidelines. 24 h post-transfection, total RNA was extracted, and the silencing efficiency of each siRNA was evaluated via RT-qPCR. The siRNA with the most effective Yap1 mRNA knockdown was chosen for further experiments. Finally, Yap1-si-3 was chosen as the best gene-silencing siRNA: ACUUGGAGGCGCUCUUCAAUGTT (sense), CAUUGAAGAGCGCCUCCAAGUTT (antisense).

mRNA transcriptome sequencing of BMDMs and bioinformatics analysis

Primary BMDMs were isolated and seeded in 6-well plates at a density of 5×10^6 cells per well, followed by a 24-h culture period. Macrophages with deficient efferocytosis were generated by treating them with 100 ng/mL of LPS. The intervention group received concurrent incubation with MSC-EVs at a concentration of 10^4 particles per cell. Cells from both groups were collected after 24 h, and total RNA was extracted using TRIzol reagent, then stored at -80 °C. mRNA sequencing was subsequently performed with technical support from Genekinder Medicaltech (Shanghai, China). The R package DESeq2 was utilized to identify differentially expressed genes (DEGs)[25]. mRNAs with $|\log_2(\text{Fold Change})| > 1.5$ and false discovery rate (FDR) < 0.05 were selected for further analysis. Expression patterns of genes associated with efferocytosis and inflammation across experimental groups were visualized using heatmaps, created with the ggplot2 and heatmap R packages.

RT-qPCR

Total RNA was extracted from BMDMs, chondrocytes, or mouse knee joint tissues using Magen Biotechnology Co., Ltd. (R4122-02). RNA purity and concentration were assessed using a NanoDrop spectrophotometer (Thermo Fisher Scientific, USA), employing the A260/A280 ratio for quality evaluation. RNA (1 μg) was converted to cDNA using the HiScript® III RT SuperMix for quantitative PCR (qPCR) Kit (Vazyme, R323-01) in a thermal cycler. qPCR was conducted with SYBR qPCR Master Mix (Q711-02, Vazyme) on an Applied Biosystems Real-Time PCR system. The expression levels of the target genes Gas6, Mertk, Stab2, Lamp1, SIRPa, Cd300a, Inos, Il1b, Il10, Arg1, Yap1, Arhgap24, Nfia, Nfib, Smad7, Tgfbi, Bax, Bcl2, Col2a1, and MMP3 were analyzed using GAPDH as the endogenous control. Relative mRNA expression was quantified using the 2-ΔΔCt method, with target gene threshold cycle (Ct) values normalized to GAPDH and fold changes assessed against the control group. All primers were designed and synthesized by Shanghai BioTNT Co., Ltd.

Dual luciferase report assay

The binding sequences between miR-21a-5p and Yap1 were initially predicted using bioinformatic tools. BioTNT Co., Ltd. synthesized DNA fragments of the wild-type (WT) and mutant (MUT) 3'-untranslated region (3'-UTR) of mouse Yap1, which include potential miR-21a-5p binding sites. These fragments were cloned into the pmirGLO dual-luciferase vector (Promega), featuring both firefly and Renilla luciferase reporter genes. The MUT construct involved mutating the seed region of the miR-21a-5p binding site to eliminate the interaction. Using Lipofectamine™ 3000 (Invitrogen), HEK293T cells were co-transfected with the constructs and miR-21a-5p mimics. Luciferase activity was assessed after 48 h using the Dual-Luciferase® Reporter Assay System (Promega), with Renilla luciferase values serving as normalization controls.

EVs vesicles from human synovial fluid

Human synovial fluid-derived extracellular vesicles (SF-EVs) were isolated using differential and ultracentrifugation methods as previously outlined[26]. Fresh synovial fluid samples were centrifuged sequentially at 3,000 × *g* and 10,000 × *g* to eliminate cells, debris, and particulates. The clarified supernatant was filtered through a 0.22 μm membrane and then ultracentrifuged at 100,000 × *g* for 120 min. The EV pellet was resuspended in sterile PBS for immediate downstream analysis or stored at -80 °C for later use. The isolated vesicles were referred to as SF-EVs.

Total miRNA was extracted from the isolated SF-EVs using a Magnetic EV miRNA Kit (TIANGEN Biotech, Beijing, China) following the manufacturer's instructions. miRNAs were reverse-transcribed with the Evo M-MLV RT Premix for qPCR, followed by RT-qPCR using the SYBR Green Premix Pro Taq HS qPCR Kit, both from Accurate Biology, China.U6 served as the internal reference for normalizing miRNA levels. The 2-ΔΔCt method was employed to determine the relative expression of miR-21a-5p.

miRNA fluorescence *in situ* hybridization

Servicebio (Wuhan, China) designed and synthesized miR-21a-5p probes. Mouse knee joint tissue sections underwent fluorescence *in situ* hybridization (FISH) using a commercial kit (GF002-50T, Servicebio) following the manufacturer's instructions. In human synovial tissue, miR-21a-5p was identified with a FAM-labeled probe, resulting in a green fluorescence signal. For mouse knee synovial tissue and subchondral bone marrow tissue, a Cy3-labeled miR-21a-5p probe was used, producing a red fluorescence signal. Servicebio (Wuhan, China) designed and synthesized the probes. Imaging was performed using a Nikon A1Si laser scanning confocal microscope (Nikon Instruments, Japan), and images were analyzed with Image-Pro Plus 6.0 software (NIH, USA). Results are expressed as relative fluorescence intensity, as described in previous study[27].

Protein extraction and western blot

Protein extraction from chondrocytes, BMSCs, and MSC-EVs under different treatments was performed using radioimmunoprecipitation assay (RIPA) lysis buffer (G2002, Solarbio) with added phosphatase inhibitor cocktail (G2007, Bimake, USA) and protease inhibitor (G2008, Solarbio). Western blotting was performed following established protocols[22]. Primary antibodies included: CD81 (GB111073, Servicebio), CD63 (GB115712, Servicebio), TSG101 (GB150022, Servicebio), Calnexin (GB111369, Servicebio), Collagen II (GB11021, Servicebio), SOX9 (GB11208, Servicebio), MMP13 (#AF5355, Affinity), TRPV1 (680834, Zenbio), MMP3 (#AF0217, Affinity), BAX (#AF0120, Affinity), Bcl2 (#AF6139, Affinity), YAP1 (#AF6328, Affinity), and GAPDH (#AF7021, Affinity).Protein bands were visualized using a ChemiDoc XRS+ Imaging System (Tanon, China) following incubation with horseradish peroxidase-conjugated goat anti-rabbit or anti-mouse secondary antibodies (#BL003A / #BL001A, Biosharp). Quantification was performed with ImageJ software (v1.8.0). All antibodies used were commercially available.

Intra-articular injection treatment in a mouse osteoarthritis model

All animal procedures were reviewed and approved by the Animal Ethics Committee of Wuhan Servicebio Animal Experiment Center (Approval No. 2024112) and were performed in accordance with the National Institutes of Health Guide for the Care and Use of Laboratory Animals.

C57BL/6 mice, sourced from GemPharmatech Co., Ltd., were utilized in this study. An OA model was induced in 6-8-week-old mice, weighing approximately 20 *g*, through the destabilization of the medial meniscus (DMM) surgical method, as previously described[28,29]. After administering isoflurane anesthesia, a longitudinal incision was performed on the skin from the distal patella to the proximal tibial plateau of the right knee. The joint capsule medial to the patellar tendon was carefully opened, and the medial meniscus and medial meniscotibial ligament (MMTL) were visualized. The MMTL was identified and transected using microsurgical scissors, resulting in destabilization of the medial meniscus. The medial meniscus was retained *in situ* and was not excised or resected. The surgical site was disinfected with povidone-iodine after closing the joint capsule and skin. Sham-operated mice experienced identical surgical exposure and arthrotomy, except that the MMTL remained unaltered. Postoperative mice had unrestricted cage activity and free access to food and water. Four independent *in vivo* experimental designs were performed as follows.

In the experiment assessing MSC-EVs' role in BMSCs' therapeutic effects, mice were randomly divided into four groups (n = 5 per group): (1) Sham; (2) DMM + PBS; (3) DMM + BMSCs; and (4) DMM + BMSCs treated with GW4869.Mice in the DMM + PBS group received 10 μL PBS by intra-articular injection. Mice in the BMSC treatment groups received 2 × 104 BMSCs suspended in 10 μL PBS per injection. To pharmacologically reduce neutral sphingomyelinase-sensitive EV release, BMSCs were pretreated with GW4869 (10 μM) for 24 h before administration; the cells were subsequently collected, washed, and resuspended at the same cell dose as that used in the DMM + BMSC group. Treatments commenced three days post-surgery and were administered every four weeks until the experiment concluded at eight weeks. Eight weeks post-DMM surgery, mice were euthanized to collect knee-joint specimens. Samples for histological analysis underwent a 4-week fixation and decalcification process before being embedded in paraffin, sectioned, and stained for further examination.

An additional independent *in vivo* experiment was performed to directly evaluate the effect of local GW4869 administration on OA progression. Mice were randomly assigned into three groups (n = 5 per group): (1) Sham + Vehicle; (2) DMM + Vehicle; and (3) DMM + GW4869. GW4869 was dissolved in vehicle solution consisting of sterile PBS containing the appropriate solvent concentration, and 10 μL of vehicle or GW4869 solution at a final concentration of 20 μM was administered by intra-articular injection into the knee joint. Treatment was initiated 3 days after DMM surgery and repeated once weekly for 4 consecutive weeks. At 8

weeks after DMM surgery, mice were euthanized, and knee joint specimens were collected for subsequent micro-computed tomography (micro-CT), histological, and molecular analyses. This experiment was performed independently of the BMSC pretreatment with GW4869 experiment described above.

In the experiment assessing the therapeutic impact of miR-21a-5p mimics, mice were randomly divided into four groups (n = 5 each): (1) Sham + negative control (NC); (2) Sham + miR-21a-5p mimic; (3) DMM + NC; and (4) DMM + miR-21a-5p mimic. An intra-articular administration of 10 μL per knee was performed using either a miR-21a-5p mimic or a negative-control oligonucleotide (BioTNT, Shanghai) at a concentration of 2 nM. The first injection was administered on postoperative day 3 and was repeated once weekly. Eight weeks post-DMM surgery, mice were euthanized to collect knee-joint specimens. Samples for histological analysis underwent a 4-week fixation and decalcification process before being embedded in paraffin, sectioned, and stained for further examination.

An experiment was conducted to assess if miR-21a-5p inhibition affects the therapeutic efficacy of MSC-EVs *in vivo*. Mice were divided into four groups (n = 5 each): (1) Sham+MSC-EVs; (2) Sham+MSC-EVs with miR-21a-5p inhibitor; (3) DMM + MSC-EVs; and (4) DMM+MSC-EVs with miR-21a-5p inhibitor. Purified MSC-EVs were administered at a dose of 1×10^8 particles per knee. Where indicated, miR-21a-5p inhibitor (Antagomir-miR-21a-5p, 2 nM, BioTNT, Shanghai) was co-administered. The preparations were diluted to a 10 μL total volume using sterile PBS and delivered via intra-articular injection. Treatment was initiated on postoperative day 3 and repeated every four weeks. Eight weeks post-DMM surgery, mice were euthanized to collect knee-joint specimens. Samples for histological analysis underwent a 4-week fixation and decalcification process before being embedded in paraffin, sectioned, and stained for further examination.

Sample-size determination, inclusion/exclusion criteria

A formal a priori power calculation was not conducted. Sample sizes were determined based on prior studies using similar experimental OA and extracellular-vesicle interventions, as well as our previous experimental experience[26,30,31]. A minimum of three independent biological replicates was used for molecular experiments, whereas five mice per group were used for the principal *in vivo* radiological, histological, and imaging analyses. Each mouse was treated as a separate experimental unit.

Animals were eligible for analysis if they completed the assigned DMM or sham procedure and the scheduled treatment regimen and provided samples of sufficient technical quality for the prespecified endpoint. No animal attrition or exclusion occurred during the study; all animals allocated to the four *in vivo* experiments survived to the planned Week-8 endpoint and were accounted for in the analyses.

Randomization and blinding

Animals in all *in vivo* experiments were randomly assigned to experimental groups using a random-number sequence, ensuring equal numbers in each group before treatment began. The individual mouse was considered the independent experimental unit. Because the administered formulations differed among treatment groups, the investigator responsible for preparing and administering the intra-articular treatments was aware of group allocation but did not participate in subsequent outcome assessment. Following completion of the animal experiments, knee specimens, histological sections, and corresponding imaging datasets were assigned coded identification numbers that concealed surgical and treatment-group information. Investigators responsible for Micro-CT quantification, histological scoring, and quantitative image analysis were blinded to group allocation until all measurements had been completed and recorded. Group allocation was revealed only after completion of the quantitative analyses.

Radiological assessment

Eight weeks post-DMM surgery, the mice were euthanized and analyzed using the MX-20 Cabinet X-ray System (Faxitron, USA). The scan was conducted with a 10-s exposure time at a voltage of 32 kV. The articular space width in mice was assessed using X-ray radiographs. Subsequently, arthrography of the knee joint samples was performed utilizing a high-resolution micro-CT imaging system (Bruker SkyScan1276, USA). Micro-CT scanning and reconstruction results indicate measurements of articular space width, relative osteophyte volume, bone mineral density (BMD), bone volume to total volume ratio (BV/TV), and trabecular thickness (Tb.Th), trabecular number (Tb.N), and trabecular separation (Tb.Sp) were analyzed.

Hematoxylin and eosin staining and safranin O-Fast green staining

Hematoxylin and Eosin (H&E) and Safranin O-Fast Green (SO/FG) staining were utilized to assess tissue morphology and cartilage structural integrity. In this study, H&E staining was applied to assess human synovium tissue, providing detailed visualization of cellular and extracellular matrix (ECM) architecture and facilitating the identification of pathological alterations. SO/FG staining was employed to assess structural alterations in knee joint articular cartilage and osteophytes. Fixed tissue sections underwent Safranin O staining to label glycosaminoglycans in the cartilage matrix (red), followed by Fast Green counterstaining to visualize collagenous and bony elements (green). This differential staining enables clear distinction between cartilaginous and non-cartilaginous components.

IF staining

For immunohistochemical and IF analyses, human synovium and mouse knee joint tissue sections were treated with 5% bovine serum albumin (BSA) for 30 min at room temperature, followed by an overnight incubation at 4 °C with primary antibodies: CD68 (GB113150, Servicebio), iNOS (GB11119, Servicebio), TREM2 (#DF12529, Affinity), interleukin-1 beta (IL-1β) (BF8021, Affinity), MMP3 (340612, ZenBio), Collagen II (DF7561, Affinity), and YAP1 (Kerafast, #ENH001). BMDMs and chondrocytes were fixed with 4% paraformaldehyde for 10 min, permeabilized using 0.15% Triton X-100 for 5 min, and washed thrice with PBS before incubation with primary antibodies targeting Arg1 (GB111841, Servicebio), iNOS (AF5484, Affinity; R23896, Zenbio), IL-1β (DF12084, Affinity), MMP3 (#AF0217, Affinity), Collagen II (GB11021, Servicebio), and YAP1 (#AF6328, Affinity). After washing with TBST (G0004, ServiceBio), samples were incubated with species-appropriate secondary antibodies conjugated to FITC or Cy3 (GB21401, GB22301, ServiceBio). Imaging utilized a Nikon A1Si Laser Scanning Confocal Microscope (Nikon Instruments Inc., Japan), with semi-quantitative analysis performed using ImageJ software.

Terminal deoxynucleotidyl transferase-mediated dUTP nick end labeling (TUNEL) staining analysis

In vivo apoptotic cells were identified using a TUNEL assay kit (G1504, G1509, Servicebio) following the manufacturer's guidelines. Joint sections embedded in paraffin were deparaffinized using xylene and then rehydrated with a graded series of ethanol. Sections were fixed in 4% paraformaldehyde for 20 min at room temperature and then permeabilized using 0.1% Triton X-100. For chondrocyte samples, permeabilization was conducted following fixation with 4% paraformaldehyde. All sections underwent a 15-min proteinase K treatment, followed by a 60-min incubation with the TUNEL reaction mixture, and were then counterstained with 4',6-diamidino-2-phenylindole (DAPI) for 5 min. A Nikon A1Si Laser Scanning Confocal Microscope (Nikon Instruments Inc., Japan) was used for imaging.

Statistical analysis

All statistical analyses were performed using GraphPad Prism version 10.1 (GraphPad Software, USA). *In vitro* cell-based experiments report the sample size (n) as the count of independent biological experiments, unless noted otherwise. *In vivo* experiments treated each animal as an independent experimental unit. Technical subsamples, consisting of multiple tissue sections or microscopic fields from the same animal,

were averaged to produce a single value per animal for statistical analysis. Accordingly, the reported *n* for animal experiments represents the number of independent animals rather than the number of sections or images. Continuous data are expressed as mean ± standard error of the mean (SEM). The Shapiro-Wilk test and graphical inspection were used to assess normality, while homogeneity of variance was evaluated prior to conducting parametric analysis. An unpaired two-tailed Student's *t*-test was applied for continuous outcomes between two independent groups when parametric test assumptions were met. A one-way analysis of variance (ANOVA) followed by Tukey's multiple-comparison test was employed for comparisons among more than two independent groups lacking a factorial structure. Non-parametric statistics were used to analyze ordinal histopathological scores, such as Osteoarthritis Research Society International (OARSI), synovitis, and osteophyte scores. The Mann-Whitney *U* test compared two groups, while the Kruskal-Wallis test with Dunn's post hoc analysis was applied for comparisons among multiple groups. Continuous outcomes in factorial animal experiments were analyzed using two-way ANOVA, followed by Šidák's multiple-comparison test. Summary of experimental replication and statistical analyses was presented in Supplementary Table 2. A *P* value below 0.05 was deemed statistically significant.

RESULTS

OA is associated with inflammatory macrophage states and impaired efferocytosis

To further characterize macrophage populations associated with OA progression, we reanalyzed the publicly available GSE220243 single-cell transcriptomic dataset comprising 26 samples[20]. Based on established marker-gene expression profiles[3,4,32], cells from control and OA samples were classified into 14 major cell populations, comprising a total of 182,943 cells [Supplementary Figure 2A]. The relative distribution of these cell populations between the control and OA groups was also examined [Supplementary Figure 2B]. The identified cell clusters including seven chondrocyte subgroups, endothelial cells, epithelial cells, granulocyte-monocyte progenitors (GMPs), macrophages, natural killer T cells (NKT), smooth muscle cells (SMCs), and T cells, and their cell markers were also visualized [Supplementary Figure 2C]. We next examined the pseudotemporal trajectory of the chondrocyte subpopulations. Pseudotime analysis showed that Chon2 and Chon7 were predominantly distributed toward the terminal region of the inferred trajectory [Supplementary Figure 2D]. KEGG pathway analysis identified enrichment of apoptosis-related signaling pathways in the two clusters [Supplementary Figure 2E and F], aligning with previous findings that associate chondrocyte apoptosis with OA progression[33-35].

Efferocytosis, the process by which macrophages clear apoptotic cells, plays a crucial role in resolving inflammation[7]. Inefficient efferocytosis hinders apoptotic-cell clearance, leading to sustained inflammatory signals and synovial inflammation[36], while effective efferocytosis reduces pro-inflammatory cytokine production and aids in resolving inflammation[37]. Given the prominent role of macrophages in the synovial microenvironment and their close association with OA progression, we next focused on macrophage heterogeneity and functional states. OA samples exhibited a higher proportion of macrophages compared to control samples [Supplementary Figure 2B].

Unbiased clustering identified seven macrophage subclusters (Mac0-Mac6) with distinct transcriptional profiles [Figure 1A-C].Particularly, these cell clusters were:Mac0 (LGMN, LYVE1, SLC40A1, LGI2, GABRB2), Mac1 (TIMD4, XPO7, CEPT1, ZNF117, MYO1G), Mac2 (FOXB, DDIT3, NXF1, PROX1, LDLR), Mac3 (COL8A1, TSHZ2, IL17D, TMEM196, CCN5), Mac4 (TNFAIP3, IL1B, IL6, CXCL2, CCL4), Mac5 (PLCG2, CSF3R, S100A9, MMP9, S100A8), and Mac6 (CLEC10A, FCER1A, ZFAND2A, CD1C, LGALS2).To explore the transcriptional relationships among these subsets, we performed pseudotime trajectory analysis using Monocle.Mac0 cells were predominantly positioned toward the beginning of the inferred trajectory, whereas Mac4 cells, characterized by high expression of inflammatory genes, were enriched toward the opposite terminal region [Figure 1D-F]. Gene-signature scoring revealed stronger

M2-like transcriptional features in Mac0 and more pronounced M1-like features in Mac4 [Figure 1G]. Consistently, Mac0 showed higher expression of phagocytosis- and efferocytosis-related genes, whereas Mac4 exhibited greater expression of pro-inflammatory genes [Figure 1H]. Efferocytosis scoring and KEGG pathway analysis further supported the enrichment of efferocytosis-related programs in the Mac0 cluster [Supplementary Figures 3 and 4].

The synovium is the most important macrophage-resident tissue in the knee joint[38]. Initially, we investigated synovial inflammation and macrophage phenotypes in human osteoarthritis synovial tissue. In line with earlier research[39-41], human OA synovial tissues showed pronounced synovial hyperplasia, extensive cellular infiltration, and notably higher synovitis scores than normal controls [Figure 1I and J]. We conducted a detailed analysis of macrophage accumulation and phenotypic alterations in human osteoarthritis synovial tissue. OA synovium exhibited a significant rise in CD68-positive macrophages and a greater proportion of iNOS-positive cells, primarily located in the intimal lining layer [Figure 1K-M], compared to controls. In contrast, the proportion of TREM2-positive macrophages, associated with an efferocytosis-related phenotype, was significantly reduced in OA synovium [Figure 1N and O]. Macrophage infiltration in the synovium was quantified, and the phenotypic profile of synovial tissue near the patellofemoral joint was characterized in the DMM mouse model[28]. Histological analysis revealed significant synovial thickening and increased cellularity in DMM-induced OA mice compared to sham-operated controls, along with a notably higher synovitis score [Supplementary Figure 5A and B]. IF staining demonstrated increased F4/80-positive macrophage accumulation and a higher proportion of iNOS-positive pro-inflammatory macrophages in OA synovium [Supplementary Figure 5C and D], suggesting enhanced macrophage infiltration and inflammatory activation post-DMM surgery.

Efferocytosis, the process by which macrophages clear apoptotic cells, plays a crucial role in maintaining tissue homeostasis and resolving inflammation[37]. We investigated the impact of efferocytosis on macrophage phenotype by isolating murine BMDMs and primary chondrocytes, following established protocols[35,42]. An *in vitro* co-culture system was set up using apoptotic chondrocytes, with efferocytosis either permitted or inhibited [Supplementary Figure 6A]. Apoptosis was induced in chondrocytes by TNF-α treatment.TUNEL staining indicated a dose-dependent rise in apoptotic chondrocytes, with 500 ng/mL TNF-α for 24 h chosen to create the apoptotic chondrocyte model [Supplementary Figure 6B and C]. Co-culturing with apoptotic chondrocytes led to a macrophage phenotype with decreased Il1b, Inos, and Tnfα expression and enhanced interleukin-10 (IL-10) production [Supplementary Figure 6D and E]. In contrast, blockade of efferocytosis with Annexin V[24] increased pro-inflammatory macrophage responses, including higher Il1b, Inos, and Tnfα expression and increased IL-1β production [Supplementary Figure 6D and E]. These findings suggest that effective clearance of apoptotic chondrocytes is linked to a pro-resolving macrophage phenotype, while impaired efferocytosis promotes inflammatory activation.

BMSCs enhance macrophage efferocytosis and inflammation resolution through MSC-EV-mediated mechanisms

BMSCs exhibit potent immunomodulatory properties and can promote macrophage polarization toward a reparative phenotype[43,44]. However, their effects on macrophage efferocytosis remain poorly understood. Given their role in inflammation resolution and tissue homeostasis, BMSCs may provide a means of restoring impaired efferocytosis under inflammatory conditions.

We isolated BMSCs from 1-month-old C57BL/6 mice to study their impact on macrophage efferocytosis, following established methods[45] [Figure 2A]. Microscopic examination showed that the cells displayed a characteristic spindle-shaped morphology [Figure 2B]. Flow cytometry analysis confirmed the BMSC phenotype, revealing high expression levels of CD44 (99.9%), CD29 (99.8%), and CD90 (96.9%), alongside

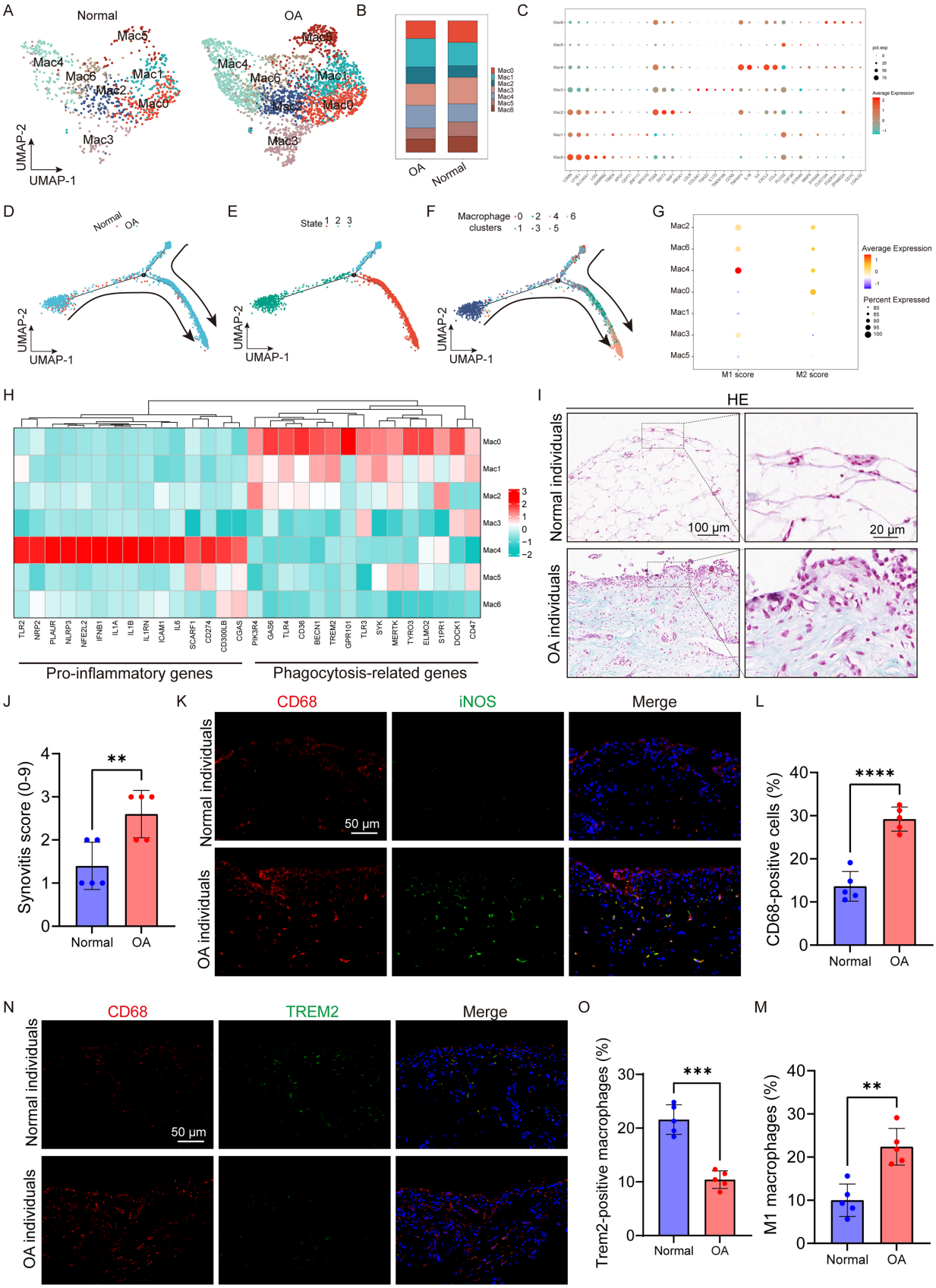


Figure 1. Impaired macrophage efferocytosis and inflammation activation during OA development. (A) UMAP plot showing seven macrophage populations (Mac0-Mac6) obtained by unsupervised clustering of macrophages from the human articular cartilage and meniscus scRNA-seq dataset GSE220243. Each dot represents one cell and is colored according to cluster identity; (B) Distribution of the seven macrophage subsets in normal and OA samples; (C) Dot plot illustrating representative marker genes for each macrophage subset. Dot size denotes the percentage of cells expressing the indicated gene, whereas color intensity indicates the relative expression level; (D-F) Pseudotime trajectory analysis depicting macrophage transitions according to cluster identity and inferred differentiation state. Mac4

cells were mainly enriched at the terminal region of the trajectory; (G) Comparison of macrophage subcluster gene signatures with canonical M1- and M2-associated transcriptional programs. Bubble size reflects the proportion of differentially expressed genes contributing to enrichment, and color indicates the direction and FDR significance of enrichment (red denotes enrichment of upregulated genes, whereas blue denotes enrichment of downregulated genes); (H) Heatmaps displaying the expression patterns of pro-inflammatory and phagocytosis/efferocytosis-associated genes across macrophage subsets, with tile color representing relative expression abundance; (I and J) Representative H&E-stained sections of human synovium and corresponding synovitis scores in normal and OA groups (n = 5 independent human donors per group). Scale bars: 20 and 100 μm; (K) Representative immunofluorescence images of CD68 and iNOS expression in normal and OA human synovial tissues. Scale bar: 50 μm; (L and M) Quantification of CD68-positive macrophages and iNOS-positive pro-inflammatory macrophages, respectively (n = 5 independent human donors per group); (N) Representative immunofluorescence images showing CD68 and TREM2 staining in normal and OA human synovial tissues. Scale bar: 50 μm; (O) Quantification of TREM2-positive macrophages (n = 5 independent human donors per group). Statistical analysis was performed using an unpaired Student's t-test for (L), (M), and (O), and the Mann-Whitney U test for (J). $^{*}P < 0.05$, $^{**}P < 0.01$, $^{***}P < 0.001$, $^{****}P < 0.0001$. OA: Osteoarthritis; UMAP: uniform manifold approximation and projection; scRNA-seq: single-cell RNA sequencing; FDR: false discovery rate; H&E: hematoxylin and eosin; iNOS: inducible nitric oxide synthase; TREM2: triggering receptor expressed on myeloid cells 2.

minimal expression of CD45 (0.37%) and CD11b (0.24%) [Figure 2C]. We then established a BMSC-macrophage co-culture model with or without LPS stimulation6[6] [Supplementary Figure 7A]. RT-qPCR analysis indicated that LPS decreased the expression of efferocytosis-related genes such as Gas6, Mertk, Stab2, Lamp1, Sirpα, and Cd300a; however, co-culture with BMSCs mitigated these effects [Supplementary Figure 7B].

Treatment with GW4869 attenuated the effects of BMSCs on efferocytosis-related gene expression [Supplementary Figure 7B]. Phagocytosis assays demonstrated a consistent trend [Supplementary Figure 7C and D]. Furthermore, we evaluated the inflammation modulation of BMSCs on macrophages. As expected, LPS also induced a pro-inflammatory macrophage phenotype, characterized by increased iNOS-positive cells and elevated Il1b, Tnfα, and Inos expression, together with reduced Arg1 and Il10 expression [Supplementary Figure 7E-G]. Co-culture with BMSCs significantly promoted anti-inflammatory polarization, and restored the down-regulation of anti-inflammatory factors Il10 and Arg1 induced by LPS in BMDMs [Supplementary Figure 7E-G]. However, administration of GW4869 evidently reversed the therapeutic effects of BMSCs [Supplementary Figure 7E-G].

We next isolated MSC-EVs from BMSC-conditioned medium by ultracentrifugation. TEM revealed a typical vesicular morphology [Figure 2D]. Western blot analysis verified the presence of exosomal surface markers CD81, CD63, and TSG101 in both MSC-EVs preparations [Figure 2E]. NTA indicated that the isolated MSC-EV preparations primarily exhibited a particle-size distribution between 30 and 200 nm [Figure 2F]. Then, we evaluated the effects of MSC-EVs on macrophage efferocytosis and inflammation [Figure 2G]. RT-qPCR analysis demonstrated that MSC-EVs, akin to BMSCs, reinstated the expression of efferocytosis-related genes such as Gas6, Mertk, Stab2, Lamp1, Sirpα, and Cd300a following LPS induction [Figure 2H and Supplementary Figure 8]. As expected, MSC-EVs significantly enhanced macrophage efferocytosis under LPS stimulation, as demonstrated by an increased clearance of fluorescent apoptotic cells [Figure 2I and J]. IF staining demonstrated that LPS resulted in decreased expression of Arg1 and increased expression of Inos, whereas MSC-EVs restored the expression of Arg1 [Figure 2K and L]. *In vitro* experiments with LPS-polarized M1 macrophages demonstrated that MSC-EVs modulate macrophage plasticity by downregulating pro-inflammatory genes and upregulating anti-inflammatory genes, promoting a resolution-prone phenotype [Figure 2M].

These experiments demonstrate that purified BMSC-derived EVs are sufficient to enhance macrophage efferocytosis and promote a pro-resolving inflammatory phenotype *in vitro*. MSC-EVs may promote inflammatory resolution by restoring efferocytosis-related gene expression and rebalancing macrophage polarization, indicating a novel mechanism of BMSC action. This suggests that macrophages undergo a phenotypic shift from a pro-inflammatory to an anti-inflammatory state after efferocytosis. In addition, this

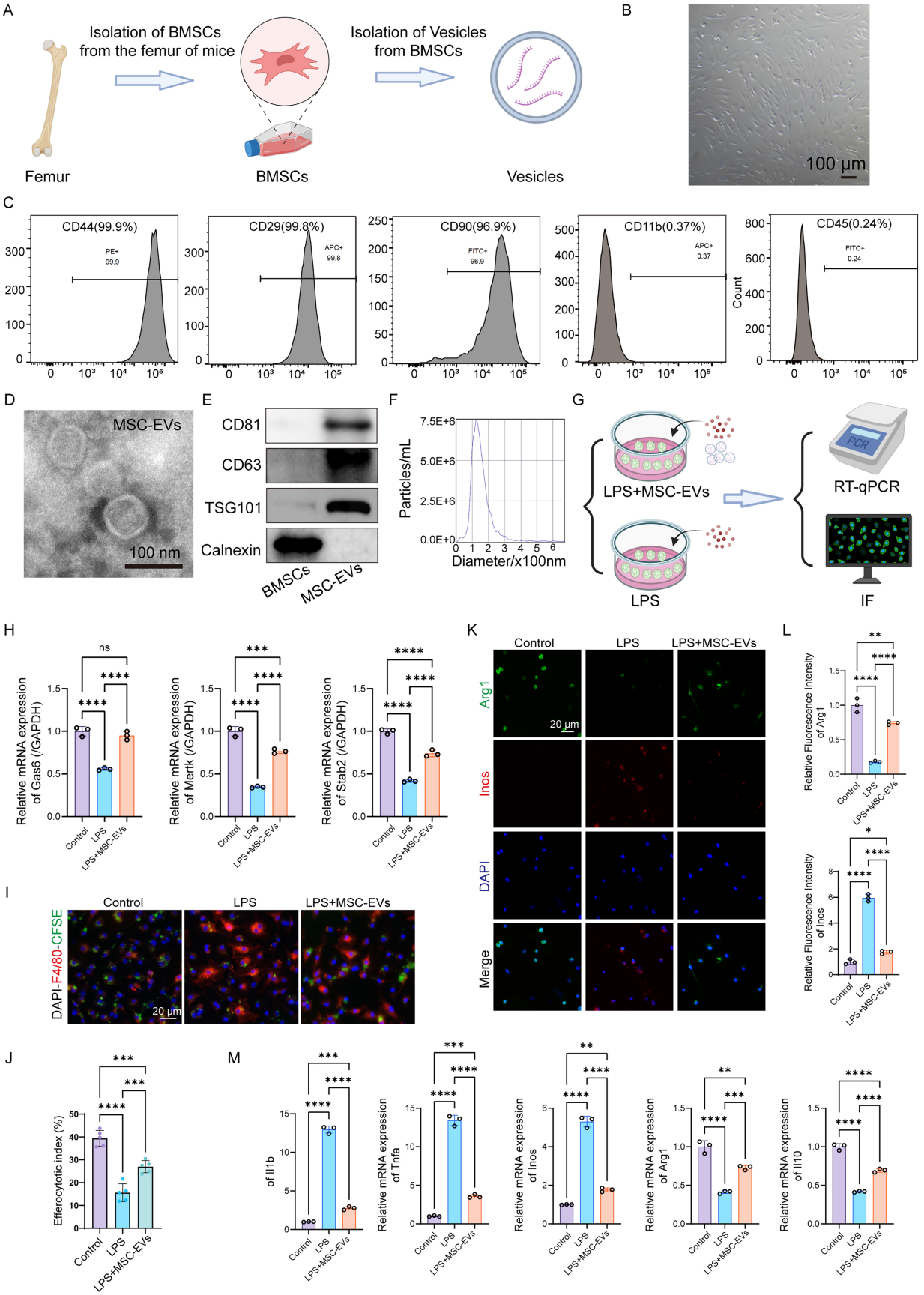


Figure 2. BMSC-derived EVs enhance macrophage efferocytosis and promote a pro-resolving phenotype *in vitro*. (A) Scheme of MSC-EVs isolation; (B) Representative microscopic image showing the characteristic spindle-shaped appearance of BMSCs; (C) Flow cytometry was performed to assess BMSC surface-marker expression. Cells were positive for CD44, CD29, and CD90 and negative for CD11b and CD45; (D) Representative TEM image showing the morphology of MSC-EVs. Scale bar: 100 nm; (E) Western blot analysis of characteristic MSC-EV protein markers; (F) Size distribution of MSC-EVs determined by NTA; (G) Schematic overview of the experimental design used to

evaluate the effects of MSC-EVs on macrophages exposed to LPS (100 ng/mL); (H) Expression of efferocytosis-associated genes in macrophages under the indicated experimental conditions was determined by RT-qPCR (n = 3 independent biological experiments); (I and J) Representative immunofluorescence images and corresponding quantification of efferocytic activity in macrophages following a 2-h co-culture with CFSE-labeled ACs (n = 5 independent biological experiments). Scale bar: 20 μm; (K and L) Representative immunofluorescence staining and quantitative assessment of Arg1 and iNOS expression in macrophages (n = 3 independent biological experiments); (M) RT-qPCR measurement of inflammation-associated genes in macrophages exposed to LPS (100 ng/mL) for 24 h in the presence or absence of MSC-EV treatment (n = 3 independent biological experiments). For (H), (J), (L), and (M), comparisons among multiple groups were performed using one-way ANOVA followed by Tukey's multiple-comparison test. $^{*}P < 0.05$, $^{**}P < 0.01$, $^{***}P < 0.001$, $^{****}P < 0.0001$. (A) and (G) were created with BioRender.com. BMSCs: Bone marrow mesenchymal stem cells; EVs: extracellular vesicles; MSC-EVs: mesenchymal stem cell-derived extracellular vesicles; TEM: transmission electron microscopy; NTA: nanoparticle tracking analysis; LPS: lipopolysaccharide; RT-qPCR: quantitative real-time polymerase chain reaction; CFSE: carboxyfluorescein succinimidyl ester; ACs: apoptotic chondrocytes; iNOS: inducible nitric oxide synthase; ANOVA: analysis of variance.

MSC-EV-associated pathway may be exploited therapeutically in inflammatory diseases where impaired efferocytosis perpetuates inflammation, such as OA.

MSC-EVs-induced enhancement of macrophage efferocytosis alleviated chondrocytes damage *in vitro*

To investigate whether MSC-EVs could mitigate chondrocyte damage through enhancing macrophage efferocytosis, we isolated murine primary chondrocytes from neonatal C57BL/6 mice[46], and co-cultured them with macrophages under varying efferocytosis conditions [Figure 3A]. Gene expression analysis revealed that chondrocytes co-cultured with macrophages with impaired efferocytosis had reduced expression of anabolic genes Sox9 and Col2a1, alongside elevated expression of catabolic genes Mmp3 and Mmp13 [Figure 3B], suggesting disrupted cartilage homeostasis. Notably, LPS-stimulated macrophages markedly upregulated Il1b expression in chondrocytes, an effect substantially reversed by MSC-EVs treatment [Figure 3C and D], underscoring the role of MSC-EVs in suppressing pro-inflammatory signaling. Further supporting this, chondrocytes co-cultured with LPS-stimulated macrophages exhibited degenerative phenotypes, including reduced Col2a1 and elevated Mmp3 expression. The LPS+MSC-EVs group showed significantly reduced effects [Figure 3E and F], indicating that MSC-EVs may preserve chondrocyte integrity by influencing macrophage behavior. Western blot analysis corroborated these findings, showing downregulation of Col2a1 and Sox9 and upregulation of Mmp3 and Mmp13 under impaired efferocytosis, which were effectively rescued by MSC-EVs [Figure 3G and H]. The restoration of anabolic-catabolic balance indicates that enhanced efferocytosis may promote a pro-resolutive macrophage phenotype capable of supporting chondrocyte viability.

Apoptosis assays further demonstrated that exposure to LPS-stimulated macrophages elevated chondrocyte apoptosis, whereas MSC-EVs treatment markedly reduced cell death [Figure 3I and J]. This protective effect underscores the therapeutic potential of MSC-EVs-mediated efferocytosis enhancement in interrupting the apoptotic-inflammation loop characteristic of OA. To delineate the role of efferocytosis in a more physiologically relevant context, we established an indirect co-culture model[24]. The experiment consisted of four groups. The lower compartment was seeded with either normal or apoptotic chondrocytes, while the upper compartment contained macrophages with normal or impaired efferocytosis [Figure 3K]. After 24 h of co-culture, apoptotic chondrocytes exhibited decreased Bcl2 and Col2a1 and increased Bax and Mmp3 expression, which was exacerbated by co-culture with efferocytosis-impaired macrophages [Figure 3L and Supplementary Figure 9]. Conversely, macrophages with enhanced efferocytosis capacity induced by MSC-EVs significantly ameliorated these apoptotic and catabolic responses [Figure 3L and Supplementary Figure 9]. Western blot demonstrated consistent results [Figure 3M and N]. The consistent findings from molecular and functional assays demonstrate that MSC-EVs restore macrophage efferocytic function, disrupting the cycle of inflammation and cartilage degradation crucial to OA progression.

Bone marrow mesenchymal stem cells enhanced macrophage efferocytosis, reduced inflammation, and mitigated chondrocyte damage *in vivo* through paracrine signaling associated with MSC-EVs

Building on promising *in vitro* results where MSC-EVs improved macrophage efferocytosis and reduced chondrocyte damage, we next evaluated their therapeutic effects *in vivo* using a murine DMM-induced OA model[30] to investigate whether the observed cytoprotective and anti-inflammatory effects of MSC-EVs could translate into functional preservation of joint architecture and reduction in disease progression [Figure 4A]. Sham mice underwent exposure of the joint capsule only. The mice were allocated to four groups: Sham, DMM + PBS, DMM + BMSC, and DMM + GW4869-treated BMSC. At 8 weeks after surgery, micro-CT analysis revealed marked structural deterioration in the DMM + PBS group, including a significant increase in osteophyte volume and calcified tissue formation [Figure 4B and C, Supplementary Figure 10]. In contrast, BMSC administration markedly mitigated these OA-associated structural changes, resulting in reduced osteophyte formation and ectopic calcification. These findings indicate that BMSC treatment partially preserves joint structural integrity during DMM-induced OA progression. However, pretreatment of BMSCs with GW4869, a neutral sphingomyelinase inhibitor commonly used to reduce the release of certain EV populations, significantly attenuated the structural benefits associated with BMSC administration [Figure 4B and C]. Histopathological evaluation by H&E and SO/FG further supported the micro-CT findings [Figure 4D and E]. Compared with the DMM + PBS group, mice receiving BMSCs exhibited better-preserved cartilage architecture, with reduced surface discontinuity, fewer vertical fissures, less cartilage erosion, and attenuated structural deformation. Consistently, semiquantitative assessments showed significantly lower OARSI, osteophyte, and synovitis scores in the DMM + BMSC group. These histopathological improvements were attenuated when BMSCs were pretreated with GW4869. These findings are consistent with earlier research highlighting the significance of MSC-derived MSC-EVs in cartilage regeneration and subchondral bone remodeling[47-49]. Inhibition of exosome secretion by GW4869 diminished the arthroprotective effects of BMSCs, leading to the reappearance of pathological features similar to those in OA controls. Together with the direct MSC-EV treatment experiments, the attenuation of BMSC-mediated therapeutic effects following GW4869 pretreatment supports an important role of EV-mediated paracrine signaling in the protective effects of BMSCs[50].

IF staining of synovial tissue revealed markedly increased iNOS expression in DMM-induced OA mice [Figure 4F and G], indicating enhanced synovial inflammatory activation. BMSC administration significantly reduced iNOS expression, whereas this effect was attenuated by GW4869 pretreatment. TUNEL staining further showed increased chondrocyte apoptosis in OA cartilage, which was reduced by BMSC treatment but partially restored following GW4869 pretreatment [Figure 4H and I]. Evaluation of ECM homeostasis revealed that OA mice exhibited decreased Aggrecan alongside elevated Mmp3 expression [Figure 4J and K], indicating a catabolic shift and loss of matrix integrity. BMSC administration effectively restored this imbalance, promoting an anabolic environment conducive to cartilage preservation. The reversal of this effect with GW4869 supports that MSC-EVs are pivotal in mediating ECM remodeling. Consistent with the results of H&E and SOFG staining, the administration of GW4869 suppressed the therapeutic effects of BMSCs [Figure 4J-L].

Furthermore, gene expression analysis of synovial tissue revealed reduced expression of the efferocytosis-related genes *Gas6, Mertk,* and *Stab2* in OA mice [Figure 4M], consistent with impaired apoptotic-cell clearance and sustained inflammation[7]. These changes were accompanied by increased Inos and Il1b expression and reduced Il10 expression, indicating a pro-inflammatory synovial environment. BMSC treatment partially restored the expression of efferocytosis-related and inflammatory genes, whereas these effects were attenuated by GW4869 pretreatment. Together, these findings support a contribution of EV-associated paracrine signaling to BMSC-mediated regulation of macrophage efferocytosis and inflammatory phenotype in OA.

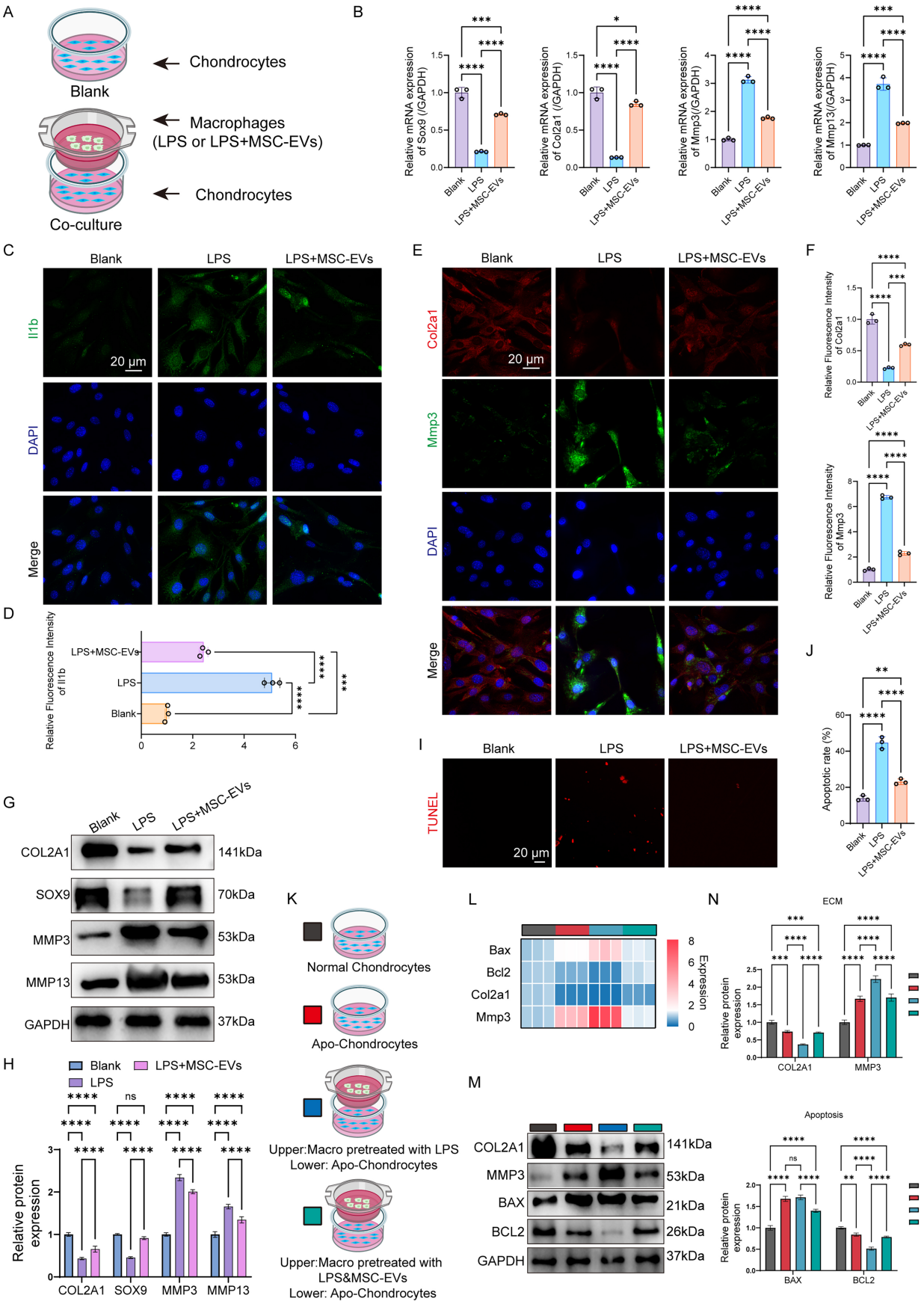


Figure 3. MSC-EV-induced enhancement of macrophage efferocytosis alleviates chondrocyte damage *in vitro*. (A) Illustration of the experiments to investigate the effects of macrophages treated with LPS (100 ng/mL) or MSC-EVs on chondrocytes; (B) Expression of ECM-associated genes was measured by RT-qPCR in chondrocytes co-cultured with macrophages exposed to LPS (100 ng/mL) or MSC-EVs (n = 3 independent biological experiments); (C) Representative immunofluorescence images showing Il1b expression in chondrocytes after co-culture with macrophages under the indicated treatments. Scale bar: 20 μm; (D) Quantitative assessment of Il1b expression in

chondrocytes (*n* = 3 independent biological experiments); (E) Representative immunofluorescence images illustrating Col2a1 and Mmp3 expression in chondrocytes co-cultured with macrophages following LPS (100 ng/mL) or MSC-EV treatment. Scale bar: 20 μm; (F) Quantitative evaluation of Col2a1 and Mmp3 expression in chondrocytes (*n* = 3 independent biological experiments); (G) Representative Western blot images showing COL2A1, SOX9, MMP3, MMP13, and GAPDH protein levels in chondrocytes co-cultured with macrophages under the indicated experimental conditions; (H) Densitometric analysis of COL2A1, SOX9, MMP3, MMP13, and GAPDH protein expression (*n* = 3 independent biological experiments); (I) Representative TUNEL-stained images of chondrocytes following co-culture with macrophages treated with LPS (100 ng/mL) or MSC-EVs. Scale bar: 20 μm; (J) Quantitative analysis of TUNEL-positive chondrocytes (*n* = 3 independent biological experiments); (K) Schematic representation of the experimental design used to examine the effects of LPS- or MSC-EV-treated macrophages on normal and apoptotic chondrocytes; (L) Heat map showing the relative gene expression of Bax, Bcl2, Col2a1, and Mmp3 in chondrocytes; (M) Representative Western blot for COL2A1, BAX, MMP3, BCL2, and GAPDH in chondrocytes co-cultured with macrophages with varying treatments; (N) Quantification of COL2A1, BAX, MMP3, BCL2, and GAPDH in chondrocytes (*n* = 3 independent biological experiments). One-way ANOVA followed by Tukey's multiple-comparison test was used for comparison in multiple groups (B), (D), (F), (H), (J) and (N). $^{*}P < 0.05$, $^{**}P < 0.01$, $^{***}P < 0.001$, $^{****}P < 0.0001$. (A) and (K) were created with BioRender.com. MSC-EVs: Mesenchymal stem cell-derived extracellular vesicles; LPS: lipopolysaccharide; ECM: extracellular matrix; RT-qPCR: quantitative real-time polymerase chain reaction; TUNEL: terminal deoxynucleotidyl transferase-mediated dUTP nick end labeling; GAPDH: glyceraldehyde-3-phosphate dehydrogenase; ANOVA: analysis of variance.

miR-21a-5p is prevalent in BMSC-EVs and linked to macrophage changes related to OA

miR-21a-5p is prevalent in BMSC-EVs and linked to macrophage changes related to OA. After confirming the protective effects of BMSCs and BMSC-derived EVs in prior *in vitro* and *in vivo* studies, we explored the molecular mechanisms responsible for these effects. Given the critical role of miRNAs as key functional cargo in MSC-EV-mediated intercellular communication and regulatory functions[51], we aimed to profile the miRNA expression in EVs from BMSCs using miRNA sequencing [Figure 5A]. The data analysis identified the ten most abundant miRNAs, as depicted in Figure 5B. RT-qPCR analysis verified that miR-21a-5p, miR-5119, and miR-17-3p were the most prevalent miRNAs in MSC-EVs [Figure 5C]. miR-21a-5p was increased in macrophages following MSC-EV treatment but not following LPS stimulation alone, indicating that this increase was associated with MSC-EV exposure rather than being a nonspecific response to inflammatory stimulation [Figure 5D and E]. The findings indicated that macrophage miR-21a-5p expression was elevated due to MSC-EV exposure, not inflammatory stimuli. The significant downregulation of miR-21a-5p in synovial fluid-derived extracellular vesicles and synovial tissues from OA patients highlights its clinical relevance and suggests a potential deficiency in miR-21a-5p-mediated regulatory mechanisms in OA [Figure 5F-H].

Co-culture with BMSCs increased miR-21a-5p abundance in macrophages, whereas this increase was attenuated by GW4869 pretreatment of BMSCs [Figure 5I and J]. The enrichment of miR-21a-5p in BMSC-EVs supports the role of EV-associated intercellular signaling. The enrichment of miR-21a-5p in MSC-EVs suggests a link between EV-related intercellular signaling and elevated miR-21a-5p levels in recipient macrophages, despite the absence of direct evidence for EV-mediated transfer in this study. *In vivo*, suppression of MSC-EVs production via local administration of GW4869 (20 μM, 10 μL per joint, once a week for four weeks)[26] significantly reduced miR-21a-5p levels in mouse synovial tissues [Figure 5K and L], and *in situ* hybridization revealed its prominent expression in subchondral bone marrow, a major niche of BMSCs, and cartilage tissue with notable reduction in OA mice [Figure 5M and N]. Collectively, these findings support an association between MSC-EV signaling and increased miR-21a-5p availability in recipient macrophages. Functional experiments further indicate that miR-21a-5p contributes to the regulation of macrophage efferocytosis and inflammatory phenotype. Its deficiency in OA synovium may thus partly explain the observed impairment in efferocytosis and sustained inflammation. The ability of MSC-EVs to replenish miR-21a-5p levels provides a plausible mechanism for their therapeutic effects in recipient macrophages. In fact, previous studies have reported that MSC-derived EV/exosomal miR-21a-5p exerts protective effects in inflammatory and tissue-injury settings, including regulation of macrophage polarization and attenuation of tissue damage[13,52].

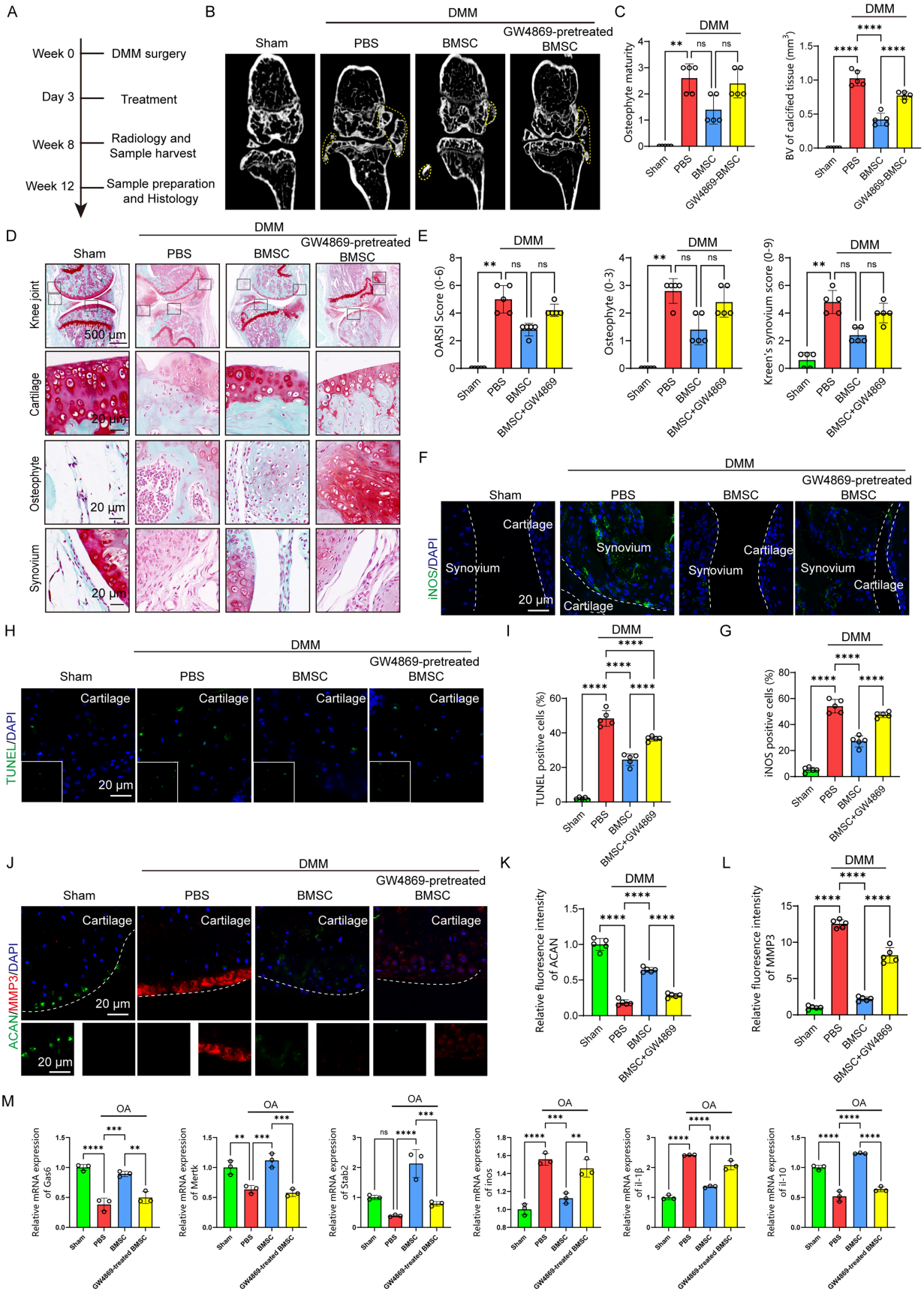


Figure 4. MSC-EVs improved macrophage efferocytosis, inflammation activation, and chondrocyte damage *in vivo*. (A) Schematic timeline of the *in vivo* experiment designed to assess whether BMSCs modulate macrophage efferocytosis, inflammatory responses, and cartilage injury through MSC-EV-associated mechanisms; (B and C) Representative micro-CT images of mouse knee joints and corresponding quantitative evaluation of osteophyte formation. Osteophytes are highlighted in yellow (n = 5 mice per group); (D) Representative SO/FG-stained sections of knee joints from mice receiving BMSC or GW4869 treatment. Scale bars: 1,500 and 20 μm; (E) Quantitative

assessment of OARSI, synovitis, and osteophyte scores based on SO/FG-stained sections (n = 5 mice per group); (F) Representative immunofluorescence images showing iNOS expression in mouse knee synovial tissue. Scale bar: 20 μm; (G) Quantification of iNOS immunofluorescence signals (n = 5 mice per group); (H) Representative TUNEL-stained images of mouse articular cartilage. Scale bar: 20 μm; (I) Quantitative analysis of TUNEL-positive cells in cartilage (n = 5 mice per group); (J) Representative immunofluorescence images showing Aggrecan and Mmp3 expression in articular cartilage. Scale bar: 20 μm; (K and L) Quantitative assessment of Aggrecan and Mmp3 immunofluorescence signals, respectively (n = 5 mice per group); (M) RT-qPCR measurement of efferocytosis- and inflammation-associated genes in mouse knee synovial tissue (n = 3 mice per group). Osteophyte maturity, OARSI, synovitis, and osteophyte scores were analyzed using the Kruskal-Wallis test followed by Dunn's multiple-comparison test. For (G), (I), (K), (L), and (M), comparisons among multiple groups were performed using one-way ANOVA followed by Tukey's multiple-comparison test. $^{*}P < 0.05$, $^{**}P < 0.01$, $^{***}P < 0.001$, $^{****}P < 0.0001$. MSC-EVs: Mesenchymal stem cell-derived extracellular vesicles; BMSCs: bone marrow mesenchymal stem cells; micro-CT: micro-computed tomography; SO/FG: Safranin O/Fast Green; OARSI: Osteoarthritis Research Society International; iNOS: inducible nitric oxide synthase; TUNEL: terminal deoxynucleotidyl transferase-mediated dUTP nick end labeling; RT-qPCR: quantitative real-time polymerase chain reaction; ANOVA: analysis of variance.

Collectively, these results position exosomal miR-21a-5p as a functional contributor through which MSC-EVs recalibrate macrophage behavior and mitigate OA-related tissue damage, providing novel insights into OA pathogenesis and opening avenues for miRNA-based therapeutics.

MSC-EVs restored the efferocytosis of macrophages and anti-inflammatory phenotype via miR-21a-5p/YAP1 axis

We conducted bulk RNA sequencing on LPS-stimulated macrophages treated with MSC-EVs to clarify the molecular mechanisms by which MSC-EVs influence macrophage function [Figure 6A]. KEGG pathway enrichment analysis revealed significant modulation of efferocytosis and inflammation-related pathways, including TNF and IL-17 signaling [Figure 6B], consistent with established pathways involved in OA progression and macrophage polarization[39,40]. Subsequent analysis demonstrated that MSC-EVs downregulated pro-inflammatory cytokines Il1b and Il6, while upregulating key efferocytosis-related genes, such as Gas6[6], Stab1[53], Trem2[53], and Cd36[53] [Figure 6C]. These results indicated a shift toward a pro-resolutive phenotype that aligns with recent findings on efferocytosis-mediated inflammation resolution[6,53]. The macrophage response to MSC-EVs diminished when BMSCs producing these EVs were transfected with a miR-21a-5p inhibitor, indicating that donor-cell miR-21a-5p functionally contributes to the MSC-EV-associated effects [Figure 6D].

To identify downstream targets of miR-21a-5p, we integrated DEGs with predictions from Elmmo, Diana_microT, and TarBase databases, identifying six candidate genes, including Smad7, Nfla, Yap1, Nflb, Arhgap24, and Tgfbi [Figure 6E]. Among the six candidate target genes (*Smad7*, *Nfla*, *Yap1*, *Nflb*, *Arhgap24*, and *Tgfbi*), only Yap1 expression was significantly reversed by miR-21a-5p inhibition following MSC-exosome treatment, supporting Yap1 as a potential downstream target of miR-21a-5p [Supplementary Figure 11]. Yap1 exhibited a significant decrease in mRNA expression after MSC-EV treatment, which was counteracted by inhibiting miR-21a-5p. Western blot analysis showed a concordant, although more modest, reduction in YAP1 protein abundance [Figure 6F and G, Supplementary Figure 12]. The difference in the magnitude of mRNA and protein changes may reflect differences in transcript and protein turnover kinetics as well as post-translational regulation of YAP1. Bioinformatic analysis predicted miR-21a-5p binding sites in the 3'UTR of Yap1, as illustrated in Figure 6H. This was corroborated by luciferase reporter assays, which demonstrated decreased activity with the WT 3'UTR upon miR-21a-5p overexpression, as shown in Figure 6I. The inverse relationship between miR-21a-5p and YAP1 was further validated by IF staining, which showed LPS-induced YAP1 upregulation was suppressed by miR-21a-5p mimics [Supplementary Figure 13A and B]. To further clarify the relationship between Yap1-related efferocytosis and inflammation phenotype in macrophages, we performed Yap1 overexpression using plasmids in macrophages. Functional studies demonstrated that while miR-21a-5p mimics restored efferocytosis in LPS-treated macrophages, overexpression of Yap1 completely abolished this effect [Figure 6J and K], indicating that YAP1 suppression is essential for miR-21a-5p-mediated functional recovery in macrophages. The miR-21a-5p/Yap1 axis was

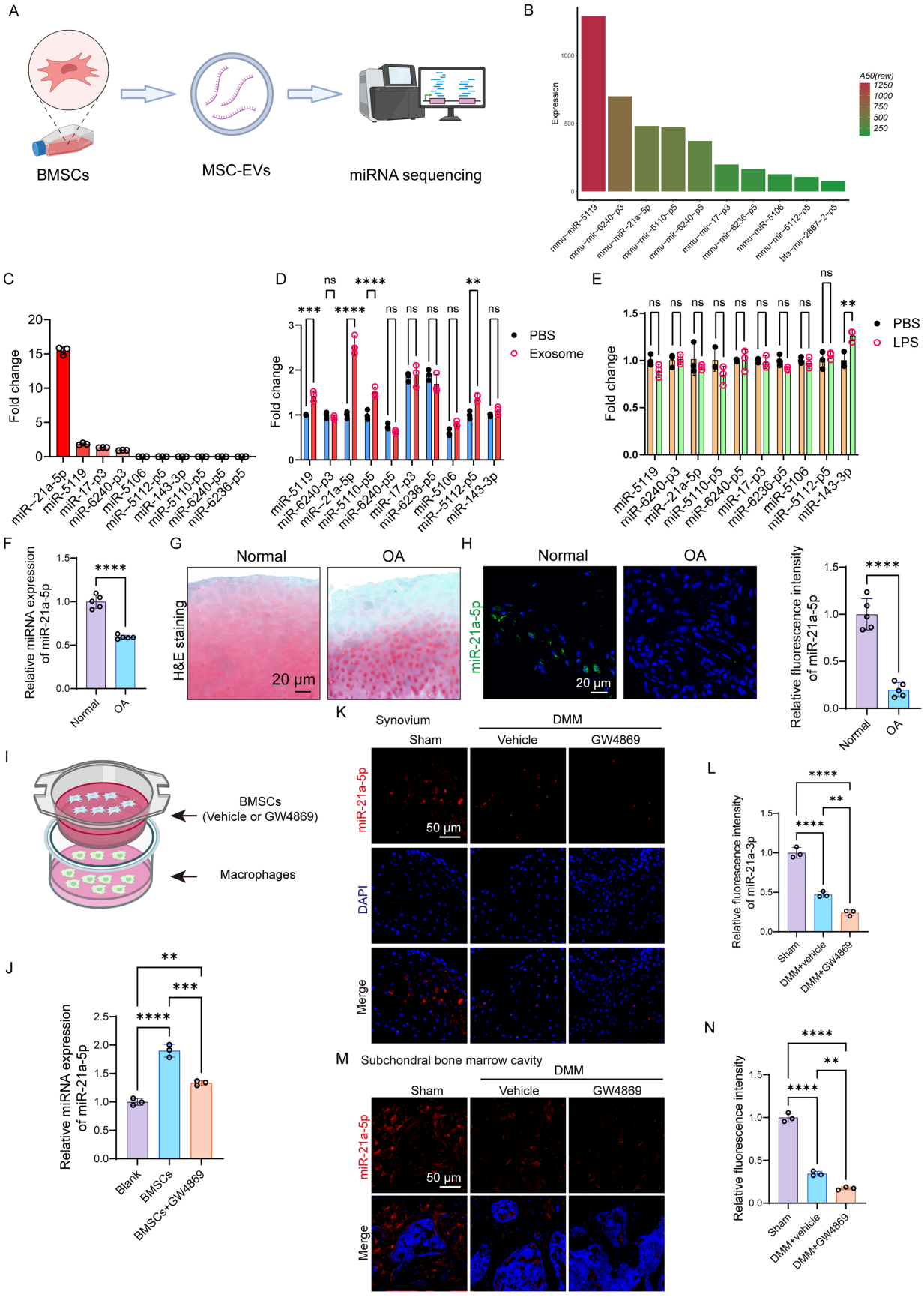


Figure 5. MSC-EVs-derived miR-21a-5p is functionally associated with OA progression and macrophage regulation. (A) Illustration of the miRNA sequencing of BMSC-derived MSC-EVs; (B) Relative proportion of miRNAs in total miRNA reads. The top 10 most abundant miRNAs in BMSC-derived MSC-EVs identified by miRNA sequencing, ranked according to normalized sequencing read abundance; (C) High expression of the top 10 miRNAs in MSC-EVs was confirmed by RT-qPCR; (D) RT-qPCR analysis of the expression of the top 10 miRNAs in macrophages stimulated with MSC-EVs for 24 h (n = 3 independent biological experiments); (E) RT-qPCR analysis of top 10

miRNAs expression in macrophages stimulated with LPS for 24 h (n = 3 independent biological experiments); (F) RT-qPCR analysis of the expression of miR-21a-5p in SF-EVs (n = 5 independent human donors per group); (G) SOFG staining of the cartilage from OA patients. Scale bars: 20 μm; (H) Representative images and quantitation results of FISH for miR-21a-5p in human OA synovial tissue (n = 5 independent human donors per group); (I) Illustration of the effect of BMSC-derived MSC-EVs on the expression of miR-21a-5p in macrophages; (J) RT-qPCR analysis of the expression of miR-21a-5p in the co-cultured macrophages (n = 3 independent biological experiments); (K and L) Representative images and quantitation results of FISH for miR-21a-5p in mouse knee synovial tissue (n = 3); (M and N) Representative images and quantitation results of FISH for miR-21a-5p in mouse subchondral bone marrow cavity (n = 3 independent biological experiments). Student's t-test was used in (D-H). One-way ANOVA followed by Tukey's multiple-comparison test was used for comparison in multiple groups (J), (L), and (N). $^{*}P < 0.05$, $^{**}P < 0.01$, $^{***}P < 0.001$, $^{****}P < 0.0001$. (A) and (I) were created with BioRender.com. MSC-EVs: Mesenchymal stem cell-derived extracellular vesicles; BMSCs: bone marrow mesenchymal stem cells; miRNA: microRNA; RT-qPCR: quantitative real-time polymerase chain reaction; LPS: lipopolysaccharide; SF-EVs: synovial fluid-derived extracellular vesicles; OA: osteoarthritis; SOFG: Safranin O-Fast Green; FISH: fluorescence *in situ* hybridization; ANOVA: analysis of variance.

shown to regulate macrophage efferocytosis and inflammation resolution, as confirmed by efferocytosis assays and RT-qPCR analysis [Figure 6J and K, Supplementary Figure 14]. This finding is particularly significant given emerging evidence that YAP/TAZ signaling promotes pro-inflammatory macrophage polarization[54,55]. Further, we evaluated the effects of Yap1 on macrophage efferocytosis and inflammation resolution [Figure 6L]. siRNA-mediated silencing of Yap1 in inflammatory macrophages enhanced efferocytosis capacity and reduced Il1b expression while increasing Mertk and Gas6 levels [Figure 6M and N], phenocopying the effects of MSC-EVs treatment and providing compelling evidence that YAP1 acts as a critical negative regulator of efferocytosis.

These findings underscore the significance of the miR-21a-5p/YAP1 axis in MSC-EV-mediated regulation of macrophage efferocytosis and inflammatory phenotype, suggesting its potential as a therapeutic target for restoring immune homeostasis in OA.

Intra-articular miR-21a-5p modulation alters OA progression *in vivo*

Building on our *in vitro* findings that highlight the role of the miR-21a-5p/YAP1 axis in controlling macrophage efferocytosis and inflammatory responses, we proceeded to investigate the impact of miR-21a-5p supplementation *in vivo*. The experimental design is shown in Figure 7A. Mice were assigned to four groups: Sham + NC, Sham + miR-21a-5p mimic, DMM + NC, and DMM + miR-21a-5p mimic. Eight weeks post-surgery, micro-CT analysis revealed no notable differences between the two sham groups. DMM mice treated with the miR-21a-5p mimic showed a significant reduction in OA-related structural changes, such as decreased osteophyte volume and less calcified tissue formation, compared to DMM + NC mice [Figure 7B and C, Supplementary Figure 15]. Histopathological analysis further showed better-preserved cartilage architecture, reduced surface fibrillation, and lower OARSI, osteophyte, and synovitis scores in the DMM + miR-21a-5p mimic group than in the DMM + NC group [Figure 7D and E].

At the molecular level, miR-21a-5p mimic treatment reduced synovial iNOS expression and decreased chondrocyte apoptosis [Figure 7F-I]. Analysis of ECM homeostasis showed reduced Aggrecan and increased MMP3 expression in DMM mice, whereas miR-21a-5p mimic administration partially restored these changes [Figure 7J-L]. In the synovium, the proportion of YAP1-positive macrophages was significantly reduced following miR-21a-5p mimic treatment [Figure 7M and N]. Consistently, gene expression analysis of synovial tissue showed increased expression of the efferocytosis-related genes Gas6, Mertk, and Stab2, together with reduced Yap1, Inos, and Il1b expression and increased Il10 expression in miR-21a-5p mimic-treated mice [Figure 7O and Supplementary Figure 16]. Collectively, these findings indicate that miR-21a-5p supplementation is associated with improved efferocytosis-related and inflammatory molecular profiles in DMM-induced OA.

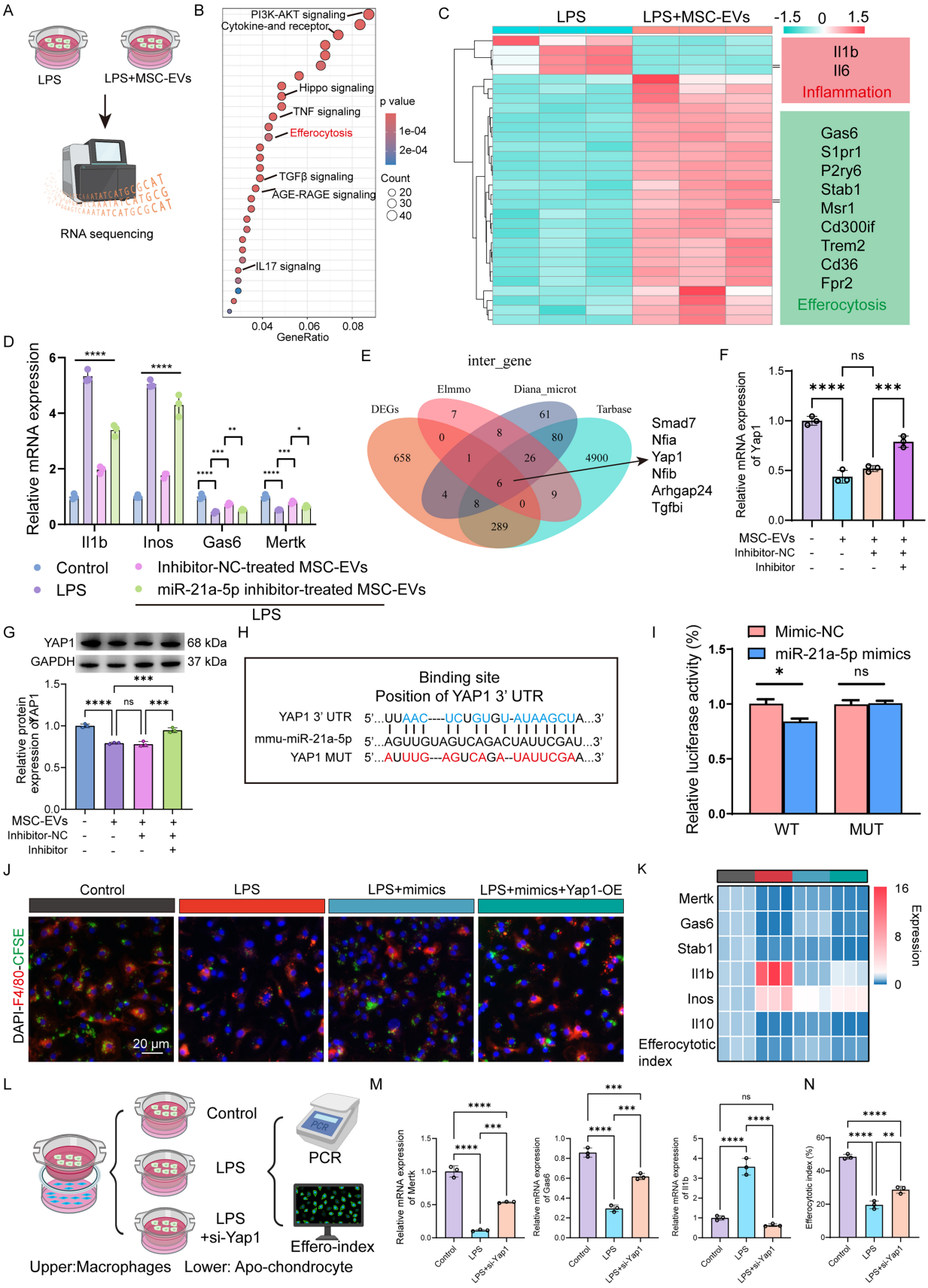


Figure 6. MSC-EVs restored the efferocytosis of macrophages and anti-inflammatory phenotype via miR-21a-5p/YAP1 axis. (A) Scheme of bulk RNA sequencing in macrophages treated with LPS or MSC-EVs; (B) KEGG pathway enrichment analysis of DEGs identified in macrophages following LPS or EV treatment; (C) Clustered heatmap illustrating altered expression patterns of genes associated with inflammation and efferocytosis in macrophages exposed to LPS or EVs; (D) Expression of inflammation- and efferocytosis-associated

genes was assessed by RT-qPCR in LPS-stimulated macrophages treated with EVs obtained from BMSCs transfected with inhibitor-NC or miR-21a-5p inhibitor (n = 3 independent biological experiments); (E) Bioinformatic prediction of candidate downstream targets of miR-21a-5p; (F) Yap1 mRNA levels were determined by RT-qPCR in macrophages receiving EVs derived from inhibitor-NC- or miR-21a-5p inhibitor-transfected BMSCs (n = 3 independent biological experiments); (G) Western blot evaluation of YAP1 protein expression in LPS-stimulated macrophages treated with EVs from BMSCs transfected with inhibitor-NC or miR-21a-5p inhibitor (n = 3 independent biological experiments); (H) Predicted complementary sequence between miR-21a-5p and its putative binding site in the Yap1 3′-UTR; (I) Dual-luciferase reporter assay evaluating the interaction between miR-21a-5p and the wild-type Yap1 3′-UTR in HEK293T cells. Co-transfection with miR-21a-5p reduced the luciferase activity of the wild-type reporter construct; (J) Representative immunofluorescence images showing F4/80-positive macrophages (red) and engulfed CFSE-labeled apoptotic chondrocytes (green) following 2 h of co-incubation under the indicated treatment conditions. Scale bar: 20 μm; (K) Heatmap summarizing inflammation- and efferocytosis-related gene-expression profiles together with the efferocytosis index across the indicated macrophage treatment groups (n = 3 independent biological experiments); (L) Schematic illustration of the macrophage-apoptotic chondrocyte co-incubation model; (M and N) RT-qPCR analysis of inflammation- and efferocytosis-related genes and efferocytotic index in macrophages with varying treatments (n = 3 independent biological experiments). NC indicated inhibitor-NC or mimic-NC. One-way ANOVA followed by Tukey's multiple-comparison test was used for comparison in multiple groups (D), (F), (G), (M), and (N). Student's t-test was used in (I). $^{*}P < 0.05$, $^{**}P < 0.01$, $^{***}P < 0.001$, $^{****}P < 0.0001$. (A) and (L) were created with BioRender.com. MSC-EVs: Mesenchymal stem cell-derived extracellular vesicles; LPS: lipopolysaccharide; KEGG: Kyoto Encyclopedia of Genes and Genomes; DEGs: differentially expressed genes; EVs: extracellular vesicles; RT-qPCR: quantitative real-time polymerase chain reaction; BMSCs: bone marrow mesenchymal stem cells; NC: negative control; 3′-UTR: 3′-untranslated region; CFSE: carboxyfluorescein succinimidyl ester; ANOVA: analysis of variance.

To further assess the functional contribution of miR-21a-5p to the *in vivo* effects associated with MSC-EV treatment, purified MSC-EVs were co-administered intra-articularly with antagomir-miR-21a-5p [Supplementary Figure 17]. At 8 weeks after surgery, micro-CT analysis revealed no significant difference between the Sham + MSC-EVs and Sham + MSC-EVs + antagomir-miR-21a-5p groups. In DMM-induced OA mice, however, co-administration of antagomir-miR-21a-5p attenuated the structural protection associated with MSC-EV treatment, as reflected by increased osteophyte volume and greater calcified tissue formation compared with the DMM + MSC-EVs group [Supplementary Figure 17B and C]. SO/FG revealed increased cartilage degeneration in mice treated with MSC-EVs and antagomir-miR-21a-5p, characterized by significant articular surface disruption and diminished cartilage integrity [Supplementary Figure 17D and E]. These findings support a functional contribution of miR-21a-5p to the protective effects associated with MSC-EV administration *in vivo*. The experiment does not confirm the EV-specific origin of the inhibited miR-21a-5p, as antagomir-miR-21a-5p was co-administered locally with MSC-EVs instead of selectively depleting miR-21a-5p from the EV preparations.

DISCUSSION

This study reveals that impaired macrophage efferocytosis is a significant aspect of OA-related immune dysfunction and demonstrates that BMSC-derived EVs can promote a pro-resolving macrophage state via the miR-21a-5p/YAP1 pathway. By integrating single-cell transcriptomics, human tissue analyses, macrophage-chondrocyte interaction models, and *in vivo* interventions, we show that OA is characterized not only by heightened macrophage inflammation but also by suppression of efferocytosis-related programs. Importantly, restoration of efferocytic capacity was accompanied by reduced inflammatory activation and improved cartilage homeostasis, linking defective apoptotic-cell clearance to sustained joint pathology. These findings collectively suggest that MSC-EVs may alleviate OA by reactivating macrophage-mediated inflammation resolution via the miR-21a-5p/YAP1 axis.

Efferocytosis facilitates the resolution of inflammation by eliminating apoptotic cells, averting secondary necrosis, and reprogramming macrophages to adopt a pro-resolving state[7]. This process is particularly relevant to OA, where chondrocyte apoptosis and persistent inflammation may reinforce each other[3,39]. Our single-cell analysis identified distinct macrophage states: Mac0 exhibited stronger efferocytosis-related and M2-like signatures, whereas Mac4 displayed a more inflammatory profile. Consistently, human OA synovium showed fewer TREM2-positive macrophages together with increased inflammatory macrophage accumulation, suggesting an imbalance between inflammation and resolution. Functionally, blockade of

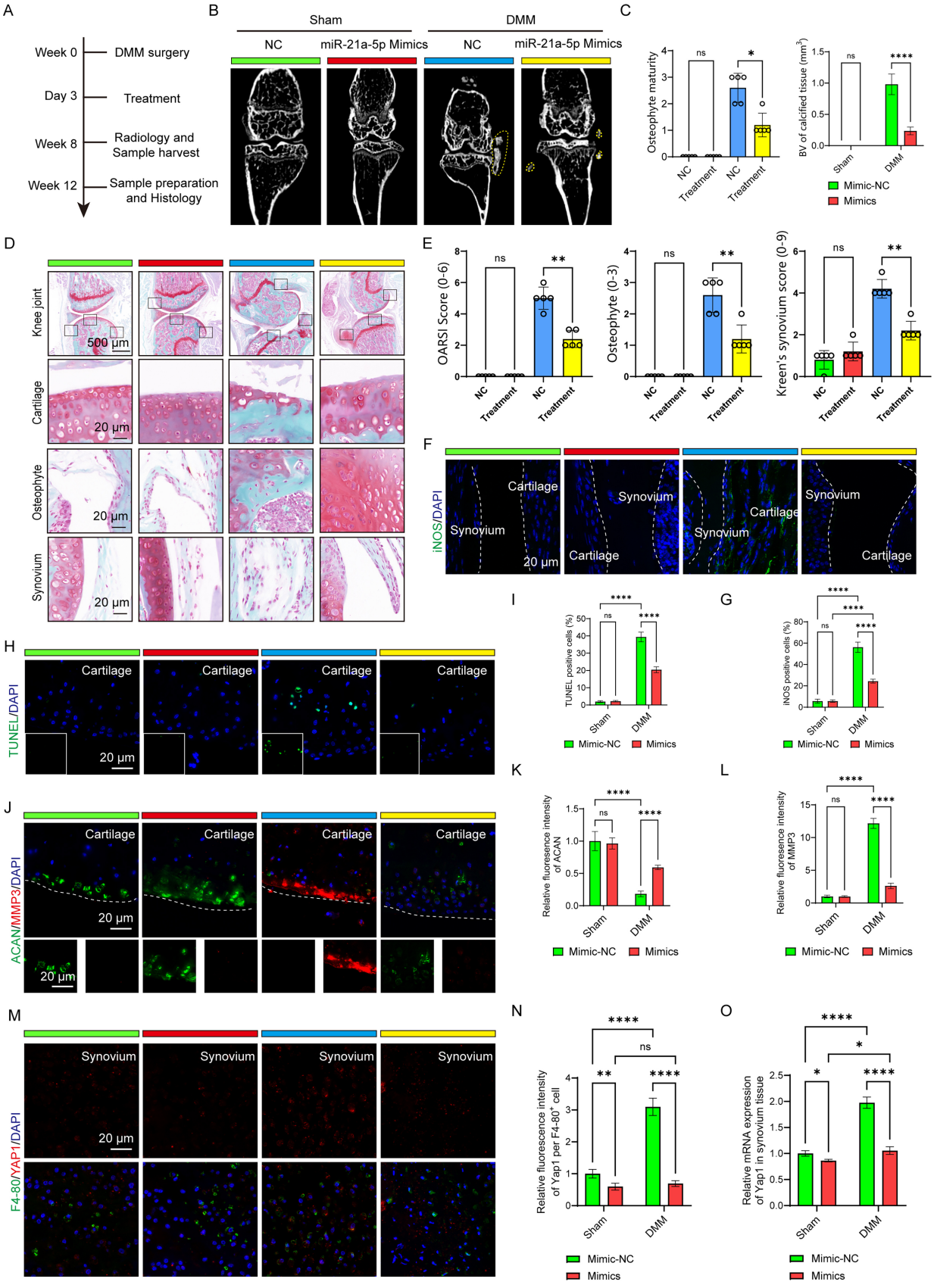


Figure 7. miR-21a-5p alleviated DMM-induced OA progression *in vivo*. (A) Schematic timeline of the *in vivo* study designed to evaluate the role of miR-21a-5p in macrophage efferocytosis, inflammatory responses, and cartilage injury; (B and C) Representative micro-CT reconstructions of mouse knee joints and corresponding assessment of osteophyte formation. Osteophytes are highlighted in yellow (n = 5 mice per group); (D) Representative SO/FG-stained sections of knee joints from mice receiving the indicated treatments with or without miR-21a-5p intervention. Scale bars: 1,500 and 20 μm; (E) Quantitative evaluation of OARSI, synovitis, and osteophyte scores based on histological staining (n = 5 mice per group); (F) Representative immunofluorescence images showing iNOS expression in mouse knee

synovial tissue. Scale bar: 20 μm; (G) Quantitative assessment of iNOS immunofluorescence signals (n = 5 mice per group); (H) Representative TUNEL-stained images of mouse articular cartilage. Scale bar: 20 μm; (I) Quantification of TUNEL-positive cells in cartilage (n = 5 mice per group); (J) Representative immunofluorescence images demonstrating Aggrecan and Mmp3 expression in mouse articular cartilage. Scale bar: 20 μm; (K and L) Quantitative measurements of Aggrecan and Mmp3 immunofluorescence signals, respectively (n = 5 mice per group); (M) Representative immunofluorescence images illustrating YAP1 expression in mouse knee synovium. Scale bar: 20 μm; (N) Quantitative analysis of YAP1 immunofluorescence intensity (n = 5 mice per group); (O) Yap1 expression in mouse knee synovial tissue was determined by RT-qPCR (n = 3 mice per group). Osteophyte maturity, OARSI, synovitis, and osteophyte scores were analyzed using the Mann-Whitney U test. Continuous outcomes involving multiple experimental groups were evaluated by two-way ANOVA followed by Šidák's multiple-comparison test. $^{*}P < 0.05$, $^{**}P < 0.01$, $^{***}P < 0.001$, $^{****}P < 0.0001$. DMM: Destabilization of the medial meniscus; OA: osteoarthritis; micro-CT: micro-computed tomography; SO/FG: Safranin O/Fast Green; OARSI: Osteoarthritis Research Society International; iNOS: inducible nitric oxide synthase; TUNEL: terminal deoxynucleotidyl transferase-mediated dUTP nick end labeling; RT-qPCR: quantitative real-time polymerase chain reaction; NC: negative control; ANOVA: analysis of variance.

apoptotic-chondrocyte clearance enhanced macrophage inflammatory responses, whereas effective efferocytosis produced the opposite effect. These findings support defective apoptotic-cell clearance as an active contributor to persistent joint inflammation. This framework provides a mechanistic explanation for the immunomodulatory effects of MSC-EVs. Previous studies have primarily linked the therapeutic effects of MSC-EVs in OA to attenuation of inflammatory signaling, reprogramming of synovial macrophage phenotypes, and restoration of cartilage matrix homeostasis[56-58]. The attenuation of BMSC-mediated protection by GW4869, together with the effects of purified MSC-EVs, further supports an important contribution of EV-associated paracrine signaling. Due to the limited specificity of GW4869 in EV secretion, these findings should be viewed as supportive rather than conclusive evidence that EVs fully explain the therapeutic effects of BMSCs. Our findings extend this paradigm by identifying restoration of macrophage efferocytosis as a previously underappreciated pro-resolving mechanism through which MSC-EVs may interrupt persistent joint inflammation and cartilage degeneration.

Mechanistically, our data implicate the miR-21a-5p/YAP1 axis in MSC-EV-mediated regulation of macrophage efferocytosis. Previous studies have established miR-21/miR-21a-5p as an important regulator of macrophage inflammatory plasticity. Das *et al*. showed that efferocytosis induces miR-21 in human macrophages, thereby suppressing PTEN/PDCD4-associated inflammatory signaling, increasing IL-10 production, and further promoting apoptotic-cell clearance[59]. In the context of MSC-derived EVs, Ma *et al*. reported that exosomal miR-21a-5p promoted M2 macrophage polarization and reduced macrophage infiltration in atherosclerosis through KLF6 and ERK1/2 signaling[13]. Xin *et al*. also demonstrated that MSC-EV-associated miR-21a-5p contributed to anti-inflammatory microglial/macrophage polarization and neuroprotection after neonatal hypoxic-ischemic injury[52]. Our findings extend its role to efferocytosis. We found that donor-cell miR-21a-5p inhibition weakened the effects of EV preparations on efferocytosis-related and inflammatory gene expression, whereas miR-21a-5p supplementation improved OA-associated changes *in vivo*. conversely, local miR-21a-5p inhibition attenuated MSC-EV-mediated structural protection. These data support a functional association between miR-21a-5p and the macrophage-regulatory effects observed with MSC-EV treatment. However, the mechanistic interpretation of EV-associated miRNA signaling requires caution. Recent critical analyses of MSC-derived small extracellular vesicles have questioned whether native EV-associated miRNAs are present and functionally delivered at sufficient stoichiometry to account for the full biological activity of MSC-EVs. In particular, Tan and Lim highlighted that individual miRNAs may occur at very low copy numbers in native mesenchymal stem cell-derived small extracellular vesicles (MSC-sEV) preparations and that cellular uptake of EVs does not necessarily result in efficient cytosolic cargo delivery, because a substantial proportion of internalized vesicles may remain within the endosomal-lysosomal system rather than undergoing productive endosomal escape[60]. These concerns are consistent with a study showing that individual abundant miRNAs can be present at substantially less than one copy per vesicle on average and with experimental evidence indicating that EV internalization does not invariably translate into functional miRNA delivery to recipient cells[61]. Therefore, our findings should

not be interpreted as demonstrating that EV-delivered miR-21a-5p is the quantitatively dominant or exclusive mediator of MSC-EV activity. Rather, they support the miR-21a-5p/YAP1 axis as one functionally relevant component of a broader, potentially multifactorial EV-associated signaling network that may also involve proteins, lipids, and other nucleic acids. Direct quantification of miR-21a-5p copy number per EV, together with particle-normalized functional comparisons and quantitative assessment of cytosolic cargo delivery, will be required to establish the stoichiometric and mechanistic contribution of EV-associated miR-21a-5p more definitively[62]. We also found YAP1 as a negative regulator of macrophage efferocytic competence, consistent with evidence linking YAP/TAZ signaling to inflammatory macrophage activation[55,63]. Given the mechanosensitive nature of YAP1, this axis may also connect MSC-EV-mediated immunoregulation with the mechanically altered OA microenvironment[64]. Further studies are needed to define how YAP1 regulates downstream efferocytic machinery.

The therapeutic significance of this axis is further corroborated by the *in vivo* effects of miR-21a-5p. Local supplementation ameliorated cartilage degeneration, osteophyte formation, synovitis, and chondrocyte apoptosis while restoring efferocytosis- and inflammation-related profiles in DMM joints. The results indicate that encouraging inflammation resolution could positively impact various joint compartments, not just the cartilage. From a translational perspective, MSC-EVs may offer a controllable, cell-free alternative to MSC transplantation, and the reduced miR-21a-5p levels observed in human OA synovial fluid EVs also suggest potential biomarker relevance. However, given the pleiotropic and context-dependent actions of miR-21a-5p, local delivery, cellular targeting, and dose optimization will be critical for future clinical translation.

It is important to recognize certain limitations. First, although donor-cell inhibition of miR-21a-5p followed by EV isolation attenuated the macrophage responses associated with BMSC-derived EVs, we did not quantitatively verify the extent of miR-21a-5p depletion within the isolated EV preparations, perform rigorous particle-matched comparisons between control and miR-21a-5p-manipulated EVs, or directly trace the intracellular delivery of EV-associated miR-21a-5p into recipient macrophages. Thus, these data support a functional contribution of miR-21a-5p to MSC-EV-associated effects but do not definitively establish EV-specific miR-21a-5p transfer as the causal mechanism. Similarly, intra-articular co-administration of antagomir-miR-21a-5p with MSC-EVs demonstrates the functional relevance of local miR-21a-5p activity but cannot distinguish EV-derived miR-21a-5p from other sources. In addition, GW4869 is not a specific or universal inhibitor of EV secretion, and GW4869-based experiments should therefore be interpreted as supportive rather than definitive evidence for EV-dependent signaling. Second, the initial EV-miRNA sequencing was exploratory and based on a single EV sample; accordingly, the identification of miR-21a-5p as a highly abundant candidate does not establish its quantitative dominance in MSC-EV activity. Other EV cargoes, as well as additional downstream targets of miR-21a-5p, may act independently or cooperatively in regulating macrophage function. Moreover, because we did not determine the absolute number of miR-21a-5p molecules per EV or the fraction of EV-associated miR-21a-5p reaching the macrophage cytosol, the stoichiometric sufficiency of EV-delivered miR-21a-5p for canonical target repression remains unresolved. Finally, the therapeutic experiments were primarily conducted in murine models with relatively small animal cohorts, and validation in larger human cohorts and additional preclinical models will be required to establish translational relevance. Future studies incorporating quantitative EV-cargo analysis, particle-normalized EV comparisons, direct cargo tracing, and orthogonal genetic approaches to EV biogenesis or release will be important for defining the EV-specific mechanism more definitively.

Collectively, our findings position macrophage efferocytosis as a potentially modifiable component of OA-associated inflammation and support MSC-EVs as a means of promoting a pro-resolving macrophage state. The miR-21a-5p/YAP1 axis represents an important component of this response, while the broader

therapeutic activity of MSC-EVs is likely to reflect a multifactorial network of EV-associated signals. This framework provides a mechanistic basis for further investigating macrophage-directed EV therapies and miRNA-based modulation of inflammation resolution in OA.

DECLARATIONS

Acknowledgments

The authors thank all the teachers at the Center for Translational Medicine of Naval Medical University who provided guidance during the development of this article. The Graphical Abstract was created with BioRender.com [Chen, Y. (2026) https://BioRender.com/lx3zsc6].

Authors' contributions

Conceptualized the study: Qian Q, Zhou Y
Developed the methodology: Han Y
Performed the software analysis: Han Y
Validated the results: Chen S
Conducted the formal analysis: Sun K
Performed the investigation: Zhang L, Han Y, Chen S
Provided resources: Fu P, Peng J, Zhou Q
Curated the data: Gong Z, Cao J
Wrote the original draft: Zhang L, Han Y
Reviewed and edited the manuscript: Qian Q, Zhou Y
Prepared the visualizations: Wang B
Supervised the study: Peng J
Acquired funding: Qian Q, Zhou Y
All authors have read and agreed to the published version of the manuscript.

Availability of data and materials

All data needed to evaluate the conclusions in the paper are present in the paper and/or the Supplementary Materials.

AI and AI-assisted tools statement

During the preparation of this manuscript, the AI tool ChatGPT (GPT-5.6 Sol) was used solely for language editing and improvement of readability. The tool did not influence the study design, data collection, analysis, interpretation, or the scientific content of the work. All authors take full responsibility for the accuracy, integrity, and final content of the manuscript.

Financial support and sponsorship

This study was supported by grants from the National Natural Science Foundation of China (Grant No. 82272471). The funders had no specific role in the conceptualization, design, data collection, analysis, decision to publish, or preparation of the manuscript.

Conflicts of interest

All authors declared that there are no conflicts of interest.

Ethical approval and consent to participate

The study involving human specimens was reviewed and approved by the Human Ethics Committee of Changzheng Hospital (Approval No. SL202410-7A). Written informed consent was obtained from all participants before sample collection. All animal procedures were reviewed and approved by the Animal Ethics Committee of Wuhan Servicebio Animal Experiment Center (Approval No. 2024112) and were performed in accordance with the National Institutes of Health Guide for the Care and Use of Laboratory Animals.

Consent for publication

Not applicable.

Copyright

© The Author(s) 2026.

Supplementary Materials

Supplementary Materials

REFERENCES

1. Robinson WH, Lepus CM, Wang Q, et al. Low-grade inflammation as a key mediator of the pathogenesis of osteoarthritis. *Nat Rev Rheumatol.* 2016;12:580-92. DOI PubMed PMC
2. O'Brien TJ, Hollinshead F, Goodrich LR. Extracellular vesicles in the treatment and prevention of osteoarthritis: can horses help us translate this therapy to humans? *Extracell Vesicles Circ Nucl Acids* 2023;4:151-69. DOI PubMed PMC
3. Ji Q, Zheng Y, Zhang G, et al. Single-cell RNA-seq analysis reveals the progression of human osteoarthritis. *Ann Rheum Dis.* 2019;78:100-10. DOI PubMed PMC
4. Fan Y, Bian X, Meng X, et al. Unveiling inflammatory and prehypertrophic cell populations as key contributors to knee cartilage degeneration in osteoarthritis using multi-omics data integration. *Ann Rheum Dis.* 2024;83:926-44. DOI PubMed PMC
5. Zhang H, Cai D, Bai X. Macrophages regulate the progression of osteoarthritis. *Osteoarthritis Cartilage.* 2020;28:555-61. DOI PubMed
6. Yao Z, Qi W, Zhang H, et al. Down-regulated GAS6 impairs synovial macrophage efferocytosis and promotes obesity-associated osteoarthritis. *Elife.* 2023;12e83069. DOI PubMed PMC
7. Doran AC, Yurdagul A Jr, Tabas I. Efferocytosis in health and disease. *Nat Rev Immunol.* 2020;20:254-67. DOI PubMed PMC
8. Li Z, Li Q, Tong K, et al. BMSC-derived exosomes promote tendon-bone healing after anterior cruciate ligament reconstruction by regulating M1/M2 macrophage polarization in rats. *Stem Cell Res Ther.* 2022;13:295. DOI PubMed PMC
9. Zhang Y, Bai J, Xiao B, Li C. BMSC-derived exosomes promote osteoporosis alleviation via M2 macrophage polarization. *Mol Med.* 2024;30:220. DOI PubMed PMC
10. Fan L, Liu C, Chen X, et al. Exosomes-loaded electroconductive hydrogel synergistically promotes tissue repair after spinal cord injury via immunoregulation and enhancement of myelinated Axon growth. *Adv Sci.* 2022;9:e2105586. DOI PubMed PMC
11. Guo J, Wang F, Hu Y, et al. Exosome-based bone-targeting drug delivery alleviates impaired osteoblastic bone formation and bone loss in inflammatory bowel diseases. *Cell Rep Med.* 2023;4:100881. DOI PubMed PMC
12. Catalano M, O'Driscoll L. Inhibiting extracellular vesicles formation and release: a review of EV inhibitors. *J Extracell Vesicles.* 2020;9:1703244. DOI PubMed PMC
13. Ma J, Chen L, Zhu X, Li Q, Hu L, Li H. Mesenchymal stem cell-derived exosomal miR-21a-5p promotes M2 macrophage polarization and reduces macrophage infiltration to attenuate atherosclerosis. *Acta Biochim Biophys Sin.* 2021;53:1227-36. DOI PubMed
14. Liu N, Ma Y, Gong W, et al. Osteocyte-derived extracellular vesicles mediate the bone-to-cartilage crosstalk and promote osteoarthritis progression. *Nat Commun.* 2025;16:4746. DOI PubMed PMC
15. Zhao J, Li X, Hu J, et al. Mesenchymal stromal cell-derived exosomes attenuate myocardial ischaemia-reperfusion injury through miR-182-regulated macrophage polarization. *Cardiovasc Res.* 2019;115:1205-16. DOI PubMed PMC
16. Xu Z, Chen Y, Ma L, et al. Role of exosomal non-coding RNAs from tumor cells and tumor-associated macrophages in the tumor microenvironment. *Mol Ther.* 2022;30:3133-54. DOI PubMed PMC
17. Zhao L, Li X, Gao M, et al. M6A modified miR-31-5p suppresses M1 macrophage polarization and autoimmune dry eye by targeting P2RX7. *Adv Sci.* 2025;12:e2415341. DOI PubMed PMC
18. Wang J, Zhang X, Zhu Y, et al. Adipocyte-derived extracellular vesicles are key regulators of central leptin sensitivity and energy homeostasis. *Cell Metab.* 2026;38:82-99.e8. DOI PubMed
19. Kumar MA, Baba SK, Sadida HQ, et al. Extracellular vesicles as tools and targets in therapy for diseases. *Signal Transduct Target Ther.* 2024;9:27. DOI PubMed PMC
20. Swahn H, Li K, Duffy T, et al. Senescent cell population with ZEB1 transcription factor as its main regulator promotes osteoarthritis in cartilage and meniscus. *Ann Rheum Dis.* 2023;82:403-15. DOI PubMed PMC
21. Smyth GK. Linear models and empirical bayes methods for assessing differential expression in microarray experiments. *Stat Appl Genet Mol Biol.* 2004;3:Article3. DOI PubMed
22. Zhao SJ, Kong FQ, Jie J, et al. Macrophage MSR1 promotes BMSC osteogenic differentiation and M2-like polarization by activating PI3K/AKT/GSK3β/β-catenin pathway. *Theranostics.* 2020;10:17-35. DOI PubMed PMC
23. Lv Z, Xu X, Sun Z, et al. TRPV1 alleviates osteoarthritis by inhibiting M1 macrophage polarization via Ca^{2+}/CaMKII/Nrf2 signaling pathway. *Cell Death Dis.* 2021;12:504. DOI PubMed PMC

24. Zhou X, Zhu D, Wu D, et al. Microneedle delivery of CAR-M-like engineered macrophages alleviates intervertebral disc degeneration through enhanced efferocytosis capacity. *Cell Rep Med.* 2025;6:102079. DOI PubMed PMC
25. Love MI, Huber W, Anders S. Moderated estimation of fold change and dispersion for RNA-seq data with DESeq2. *Genome Biol.* 2014;15:550. DOI PubMed PMC
26. Cao Y, Ruan J, Kang J, et al. Extracellular vesicles in infrapatellar fat pad from osteoarthritis patients impair cartilage metabolism and induce senescence. *Adv Sci.* 2024;11:e2303614. DOI PubMed PMC
27. Yang Y, Shen P, Yao T, et al. Novel role of circRSU1 in the progression of osteoarthritis by adjusting oxidative stress. *Theranostics.* 2021;11:1877-900. DOI PubMed PMC
28. Li J, Zhang B, Liu WX, et al. Metformin limits osteoarthritis development and progression through activation of AMPK signalling. *Ann Rheum Dis.* 2020;79:635-45. DOI PubMed PMC
29. Glasson SS, Blanchet TJ, Morris EA. The surgical destabilization of the medial meniscus (DMM) model of osteoarthritis in the 129/SvEv mouse. *Osteoarthritis Cartilage.* 2007;15:1061-9. DOI PubMed
30. Chen H, Ye T, Hu F, et al. Urchin-like ceria nanoparticles for enhanced gene therapy of osteoarthritis. *Sci Adv.* 2023;9:eadf0988. DOI PubMed PMC
31. Wilson TG, Baghel M, Kaur N, et al. Circulating miR-126-3p is a mechanistic biomarker for knee osteoarthritis. *Nat Commun.* 2025;16:2021. DOI PubMed PMC
32. Li H, Jiang X, Xiao Y, et al. Combining single-cell RNA sequencing and population-based studies reveals hand osteoarthritis-associated chondrocyte subpopulations and pathways. *Bone Res.* 2023;11:58. DOI PubMed PMC
33. Ji Z, Ren X, Jin J, et al. Injectable hydrogel encapsulating siMMP13 with anti-ROS and anti-apoptotic functions for osteoarthritis treatment. *J Nanobiotechnology.* 2024;22:466. DOI PubMed PMC
34. Hwang HS, Kim HA. Chondrocyte apoptosis in the pathogenesis of osteoarthritis. *Int J Mol Sci.* 2015;16:26035-54. DOI PubMed PMC
35. Wang BW, Jiang Y, Yao ZL, Chen PS, Yu B, Wang SN. Aucubin protects chondrocytes against IL-1β-induced apoptosis in vitro and inhibits osteoarthritis in mice model. *Drug Des Devel Ther.* 2019;13:3529-38. DOI PubMed PMC
36. Nepal S, Tiruppathi C, Tsukasaki Y, et al. STAT6 induces expression of Gas6 in macrophages to clear apoptotic neutrophils and resolve inflammation. *Proc Natl Acad Sci U S A.* 2019;116:16513-8. DOI PubMed PMC
37. Boada-Romero E, Martinez J, Heckmann BL, Green DR. The clearance of dead cells by efferocytosis. *Nat Rev Mol Cell Biol.* 2020;21:398-414. DOI PubMed PMC
38. Zhang L, Chen X, Cai P, et al. Reprogramming mitochondrial metabolism in synovial macrophages of early osteoarthritis by a camouflaged meta-defensome. *Adv Mater.* 2022;34:e2202715. DOI PubMed
39. Zhang H, Lin C, Zeng C, et al. Synovial macrophage M1 polarisation exacerbates experimental osteoarthritis partially through R-spondin-2. *Ann Rheum Dis.* 2018;77:1524-34. DOI PubMed
40. de Munter W, Geven EJ, Blom AB, et al. Synovial macrophages promote TGF-β signaling and protect against influx of S100A8/S100A9-producing cells after intra-articular injections of oxidized low-density lipoproteins. *Osteoarthritis Cartilage.* 2017;25:118-27. DOI PubMed
41. Zhou K, Yang C, Shi K, et al. Activated macrophage membrane-coated nanoparticles relieve osteoarthritis-induced synovitis and joint damage. *Biomaterials.* 2023;295:122036. DOI PubMed
42. Ma PF, Gao CC, Yi J, et al. Cytotherapy with M1-polarized macrophages ameliorates liver fibrosis by modulating immune microenvironment in mice. *J Hepatol.* 2017;67:770-9. DOI PubMed
43. Liu L, An Z, Zhang H, et al. Bone marrow mesenchymal stem cell-derived extracellular vesicles alleviate diabetes-exacerbated atherosclerosis via AMPK/mTOR pathway-mediated autophagy-related macrophage polarization. *Cardiovasc Diabetol.* 2025;24:48. DOI PubMed PMC
44. Hu H, Wang Z, Yang H, Bai Y, Zhu R, Cheng L. Hypoxic preconditional engineering small extracellular vesicles promoted intervertebral disc regeneration by activating Mir-7-5p/NF-Kb/Cxcl2 Axis. *Adv Sci.* 2023;10:e2304722. DOI PubMed PMC
45. Guo Y, Jia X, Cui Y, et al. Sirt3-mediated mitophagy regulates AGEs-induced BMSCs senescence and senile osteoporosis. *Redox Biol.* 2021;41:101915. DOI PubMed PMC
46. Geng N, Fan M, Kuang B, et al. 10-hydroxy-2-decenoic acid prevents osteoarthritis by targeting aspartyl β hydroxylase and inhibiting chondrocyte senescence in male mice preclinically. *Nat Commun.* 2024;15:7712. DOI PubMed PMC
47. Liu Y, Peng L, Li L, et al. 3D-bioprinted BMSC-laden biomimetic multiphasic scaffolds for efficient repair of osteochondral defects in an osteoarthritic rat model. *Biomaterials.* 2021;279:121216. DOI PubMed
48. Palamà MEF, Coco S, Shaw GM, et al. Xeno-free cultured mesenchymal stromal cells release extracellular vesicles with a "therapeutic" miRNA cargo ameliorating cartilage inflammation *in vitro*. *Theranostics.* 2023;13:1470-89. DOI PubMed PMC
49. Wu Y, Feng Y, Hu F, et al. Engineered stem cell clusters for extracellular vesicles-mediated gene delivery to rejuvenate chondrocytes and facilitate chondrogenesis in osteoarthritis therapy. *Adv Sci.* 2025;12:e2500964. DOI PubMed PMC

50. Chen M, Lu Y, Liu Y, et al. Injectable microgels with hybrid exosomes of chondrocyte-targeted FGF18 gene-editing and self-renewable lubrication for osteoarthritis therapy. *Adv Mater.* 2024;36:e2312559. DOI PubMed
51. Isaac R, Reis FCG, Ying W, Olefsky JM. Exosomes as mediators of intercellular crosstalk in metabolism. *Cell Metab.* 2021;33:1744-62. DOI PubMed PMC
52. Xin D, Li T, Chu X, et al. Mesenchymal stromal cell-derived extracellular vesicles modulate microglia/macrophage polarization and protect the brain against hypoxia-ischemic injury in neonatal mice by targeting delivery of miR-21a-5p. *Acta Biomater.* 2020;113:597-613. DOI PubMed
53. Gong S, Zhai M, Shi J, et al. TREM2 macrophage promotes cardiac repair in myocardial infarction by reprogramming metabolism via SLC25A53. *Cell Death Differ.* 2024;31:239-53. DOI PubMed PMC
54. Yang J, Li S, Li Z, et al. Targeting YAP1-regulated glycolysis in fibroblast-like synoviocytes impairs macrophage infiltration to ameliorate diabetic osteoarthritis progression. *Adv Sci.* 2024;11:e2304617. DOI PubMed PMC
55. Liang L, Xu W, Shen A, et al. Inhibition of YAP1 activity ameliorates acute lung injury through promotion of M2 macrophage polarization. *MedComm.* 2023;4:e293. DOI PubMed PMC
56. Zhang S, Teo KYW, Chuah SJ, Lai RC, Lim SK, Toh WS. MSC exosomes alleviate temporomandibular joint osteoarthritis by attenuating inflammation and restoring matrix homeostasis. *Biomaterials.* 2019;200:35-47. DOI PubMed
57. Zhang J, Rong Y, Luo C, Cui W. Bone marrow mesenchymal stem cell-derived exosomes prevent osteoarthritis by regulating synovial macrophage polarization. *Aging.* 2020;12:25138-52. DOI PubMed PMC
58. Wang Y, Yu D, Liu Z, et al. Exosomes from embryonic mesenchymal stem cells alleviate osteoarthritis through balancing synthesis and degradation of cartilage extracellular matrix. *Stem Cell Res Ther.* 2017;8:189. DOI PubMed PMC
59. Das A, Ganesh K, Khanna S, Sen CK, Roy S. Engulfment of apoptotic cells by macrophages: a role of microRNA-21 in the resolution of wound inflammation. *J Immunol.* 2014;192:1120-9. DOI PubMed PMC
60. Tan TT, Lim SK. Rethinking miRNAs in MSC-sEV therapeutics: implications for manufacture, mechanism of action, and development of robust potency CQAs. *Extracell Vesicles Circ Nucl Acids.* 2025;6:807-21. DOI PubMed PMC
61. Chevillet JR, Kang Q, Ruf IK, et al. Quantitative and stoichiometric analysis of the microRNA content of exosomes. *Proc Natl Acad Sci U S A.* 2014;111:14888-93. DOI PubMed PMC
62. Albanese M, Chen YA, Hüls C, et al. MicroRNAs are minor constituents of extracellular vesicles that are rarely delivered to target cells. *PLoS Genet.* 2021;17:e1009951. DOI PubMed PMC
63. Mia MM, Cibi DM, Abdul Ghani SAB, et al. YAP/TAZ deficiency reprograms macrophage phenotype and improves infarct healing and cardiac function after myocardial infarction. *PLoS Biol.* 2020;18:e3000941. DOI PubMed PMC
64. Meli VS, Atcha H, Veerasubramanian PK, et al. YAP-mediated mechanotransduction tunes the macrophage inflammatory response. *Sci Adv.* 2020;6:eabb8471. DOI PubMed PMC

Disclaimer/Publisher's Note: All statements, opinions, and data contained in this publication are solely those of the individual author(s) and contributor(s) and do not necessarily reflect those of OAE and/or the editor(s). OAE and/or the editor(s) disclaim any responsibility for harm to persons or property resulting from the use of any ideas, methods, instructions, or products mentioned in the content.

© The Author(s) 2026. Open Access This article is licensed under a Creative Commons Attribution 4.0 International License (https://creativecommons.org/licenses/by/4.0/), which permits unrestricted use, sharing, adaptation, distribution and reproduction in any medium or format, for any purpose, even commercially, as long as you give appropriate credit to the original author(s) and the source, provide a link to the Creative Commons license, and indicate if changes were made.